

Continuous Preintegration Theory for Graph-based Visual-Inertial Navigation

Kevin Eickenhoff, Patrick Geneva, and Guoquan Huang

Abstract—In this paper we propose a new continuous preintegration theory for graph-based sensor fusion with an inertial measurement unit (IMU) and a camera (or other aiding sensors). Rather than using discrete sampling of the measurement dynamics as in current methods, we analytically derive the closed-form solutions to the preintegration equations, yielding improved accuracy in state estimation. We advocate two new different inertial models for preintegration: (i) the model that assumes piecewise constant measurements, and (ii) the model that assumes piecewise constant local true acceleration. We show through extensive Monte-Carlo simulations the effect that the choice of preintegration model has on estimation performance. To validate the proposed preintegration theory, we develop both direct and indirect visual-inertial navigation systems (VINS) that leverage our preintegration. In the first, within a tightly-coupled, sliding-window optimization framework, we jointly estimate the features in the window and the IMU states while performing marginalization to bound the computational cost. In the second, we loosely couple the IMU preintegration with a direct image alignment that estimates relative camera motion by minimizing the photometric errors (i.e., raw image intensity difference), allowing for efficient and informative loop closures. Both systems are extensively tested in real-world experiments and are shown to offer competitive performance to state-of-the-art methods.

I. INTRODUCTION

Accurate localization for autonomous systems is a prerequisite in many robotic applications such as planetary exploration (Mourikis, Trawny, Roumeliotis, Johnson, and Matthies, 2007), search and rescue (Ellekilde, 2007), and autonomous driving (Geiger, Lenz, and Urtasun, 2012). In many of these scenarios, access to global information such as from a Global Positioning System (GPS), motion capture system, or a prior map of the environment is unavailable. Instead, one has to estimate the robot state and its surroundings based on noisy, local measurements from onboard sensors, by performing simultaneous localization and mapping (SLAM), which has witnessed significant research efforts in the past three decades (Cadena, Carlone, Carrillo, Latif, Scaramuzza, Neira, Reid, and Leonard, 2016).

Of many possible sensors used in SLAM, Micro-Electro-Mechanical System (MEMS) inertial measurement units (IMUs) have become ubiquitous. These low-cost and lightweight sensors typically provide local linear acceleration and angular velocity readings, and are well suited for many applications such as Unmanned Aerial Vehicles (UAVs) (Ling, Liu, and Shen, 2016) and mobile devices (Wu, Ahmed, Georgiou, and Roumeliotis, 2015). IMUs provide information only about

the derivatives of the state, so estimation must be performed by integrating over these noisy measurements. This may lead to large drifts over long periods of time, making the use of a low-cost IMU alone an unreliable solution. However, IMU readings are highly-informative about short-term motion which is ideal for fusion with measurements from exteroceptive aiding sensors, such as LiDAR and cameras. These sensors compensate for the drift issue inherent in IMUs, while high-rate inertial measurements are useful in tracking aggressive motion which may be difficult for exteroceptive low-rate sensors alone.

The canonical way of fusing IMU measurements in aided inertial navigation is to use an extended Kalman filter (EKF) (e.g., see Mourikis and Roumeliotis (2007)). In this method, the inertial measurements are used to predict to the next time instance, while measurements from exteroceptive sensors are used to update the state estimate. More recently, the development of preintegration has allowed for the efficient inclusion of high-rate IMU measurements in graph-based SLAM (Lupton and Sukkarieh, 2012; Forster, Carlone, Dellaert, and Scaramuzza, 2015, 2017). In this paper, building upon our prior conference publication (Eickenhoff, Geneva, and Huang, 2016a), we investigate in-depth the optimal use of preintegration by providing models and their analytical solutions for the preintegrated measurement dynamics, allowing for more accurate computation of the inertial factors for use in the graph optimization of visual-inertial navigation systems (VINS).

In particular, the main contributions of this work include:

- We advocate two new preintegration models (i.e., piecewise constant measurements and piecewise constant local true acceleration, instead of piecewise constant global acceleration as assumed in the existing methods) to better capture the underlying motion dynamics and offer the analytical solutions to the preintegration equations. We have open sourced the proposed preintegration to better contribute to our research community.¹
- Using the proposed continuous preintegration, we develop an indirect, tightly-coupled, sliding-window optimization based visual-inertial odometry (VIO), which marginalizes out features from the state vector when moving to the next time window to enable real-time performance of bounded computational cost.
- With the proposed continuous IMU preintegration, we further develop a loosely-coupled, direct VINS, which

The authors are with the Dept. of Mechanical Engineering, and Computer and Information Sciences, University of Delaware, Newark, DE 19716, USA. E-mail: {keck, pgeneva, ghuang}@udel.edu

¹The open source of the proposed continuous preintegration is available at: <https://github.com/rpng/cpi>

fuses the preintegrated inertial measurements with the direct image alignment results.

- We conduct thorough Monte-Carlo simulation analysis of different preintegration models by varying motion dynamics and IMU sampling rates. We perform extensive real-world experiments to validate the proposed VINS using our preintegration by comparing with a state-of-the-art method.

The remainder of the paper is organized as follows: After a brief overview of related work in the next section and estimation preliminaries in Section III, we present in detail the proposed continuous preintegration in Section IV. The direct and indirect VINS that use the proposed preintegration are described in Section V. In Sections VI and VII, we validate the proposed VINS algorithms through both simulations and experiments. Finally, Section VIII concludes the work in this paper, as well as the possible future research directions.

II. RELATED WORK

A. Visual-Inertial Navigation

Mourikis and Roumeliotis (2007) proposed one of the earliest successful VINS algorithms, known as the Multi-State Constraint Kalman Filter (MSCKF). This filtering approach used quaternion-based inertial dynamics (Trawny and Roumeliotis, 2005) for state propagation coupled with a novel update step. Rather than adding features seen in the camera images to the state vector, their visual measurements were projected onto the nullspace of the feature Jacobian matrix (akin to feature marginalization Yang, Maley, and Huang (2017)), thereby retaining motion constraints that only related to the stochastically cloned camera poses in the state vector (Roumeliotis and Burdick, 2002). While reducing the computational cost by removing the need to co-estimate features, this nullspace projection prevents the relinearization of the processed features' nonlinear measurements at later time steps.

The standard MSCKF recently has been extended in various directions. For example, Hesch, Kottas, Bowman, and Roumeliotis (2013) improved the filter consistency by enforcing the correct observability properties of the linearized EKF VINS; Guo and Roumeliotis (2013) showed that the inclusion of plane features increases the estimation accuracy; Guo, Kottas, DuToit, Ahmed, Li, and Roumeliotis (2014) extended to the case of rolling-shutter cameras with inaccurate time synchronization; and Wu, Ahmed, Georgiou, and Roumeliotis (2015) reformulated the VINS problem within a square-root inverse filtering framework for improved computational efficiency and numerical stability without sacrificing estimation accuracy. While the filtering based methods have shown to exhibit high-accuracy state estimation, they theoretically suffer from a limitation – that is, nonlinear measurements must have a *one-time* linearization before processing, possibly introducing large linearization errors into the estimator.

Batch optimization methods, by contrast, solve a nonlinear least-squares (or bundle adjustment) problem over a set of measurements, allowing for the reduction of error through relinearization (Kummerle, Grisetti, Strasdat, Konolige, and Burgard, 2011). The incorporation of *tightly-coupled* VINS

in batch optimization methods requires overcoming the high frequency nature and computational complexity of the inertial measurements.

Leutenegger, Lynen, Bosse, Siegwart, and Furgale (2015) introduced a keyframe-based VINS approach (i.e., OKVIS), whereby a set of non-sequential past camera poses and a series of recent inertial states, connected with inertial measurements, was used in nonlinear optimization for accurate trajectory estimation. These inertial factors took the form of a state prediction: every time that the linearization point for the starting inertial state changed, it is required to reintegrate the IMU dynamics. This presents inefficiencies in the inertial processing, and makes incorporating a large number of inertial factors practically infeasible.

B. Visual Processing

A key component to any VINS algorithm is the visual processing pipeline, responsible for transforming dense imagery data to motion constraints that can be incorporated into the estimation problem. Seen as the classical technique, indirect methods of visual SLAM extract and track features in the environment, while using geometric reprojection constraints during estimation. An example of a current state-of-the-art indirect method is ORB-SLAM2 (Mur-Artal and Tardós, 2017), which performs graph-based optimization of camera poses using information from 3D feature point correspondences.

In contrast, direct methods utilize raw pixel intensities in their formulation and allow for inclusion of a larger percentage of the available image information. LSD-SLAM is an example of a state-of-the-art direct visual-SLAM method which optimizes the transformation between pairs of camera keyframes based on minimizing their intensity error (Engel, Schöps, and Cremers, 2014). Note that this approach also optimizes a separate graph containing keyframe constraints to allow for the incorporation of highly informative loop-closures to correct drift over long trajectories. This work was later extended from a monocular sensor to stereo and omnidirectional cameras for improved accuracy (Engel, Stückler, and Cremers, 2015; Caruso, Engel, and Cremers, 2015). Other popular direct methods include Engel, Koltun, and Cremers (2018) and Wang, Schwörer, and Cremers (2017) which estimate keyframe depths along with the camera poses in a tightly-coupled manner, offering low-drift results.

Application of direct methods to the visual-inertial problem has seen recent attention due to their ability to robustly track dynamic motion even in low-texture environments. For example, Bloesch, Omari, Hutter, and Siegwart (2015); Bloesch, Burri, Omari, Hutter, and Siegwart (2017) used a patch-based direct method to provide updates with an iterated EKF; Usenko, Engel, Stückler, and Cremers (2016) introduced a sliding-window VINS based on the discrete preintegration and direct image alignment; Ling, Liu, and Shen (2016) employed loosely-coupled direct alignment with preintegration factors for tracking aggressive quadrotor motions. While these methods have shown the feasibility of incorporating IMU measurements with direct methods, they employed the *discrete* form of inertial preintegration.

C. Inertial Preintegration

First introduced by Lupton and Sukkarieh (2012), preintegration is a computationally efficient alternative to the standard inertial measurement integration. The authors proposed the use of discrete integration of the inertial measurement dynamics in a *local* frame of reference, preventing the need to reintegrate the state dynamics at each optimization step. While this addresses the computational complexity issue, this method suffers from singularities due to the use of Euler angles in the orientation representation. To improve the stability of this preintegration, an on-manifold representation was introduced by Forster, Carlone, Dellaert, and Scaramuzza (2015, 2017) which presents a singularity-free orientation representation on the $SO(3)$ manifold, incorporating the IMU preintegration into an efficient graph-based VINS algorithm.

While Shen, Michael, and Kumar (2015) introduced preintegration in the continuous form, they still discretely sampled the measurement dynamics without offering closed-form solutions. This left a significant gap in the theoretical completeness of preintegration theory from a continuous-time perspective. Albeit, Qin, Li, and Shen (2017) later extended to a robust tightly-coupled monocular visual-inertial localization system. As compared to the discrete approximation of the preintegrated measurement and covariance calculations used in previous methods, in our prior work (Eckenhoff, Geneva, and Huang, 2016a), we have derived the closed-form solutions to both the measurement and covariance preintegration equations and showed that these solutions offer improved accuracy over the discrete methods, especially in the case of highly dynamic motion.

In this work, based on our preliminary results (Eckenhoff, Geneva, and Huang, 2016a, 2017), we provide a solid theoretical foundation for continuous-time preintegration and show that it can be easily incorporated into different graph-based sensor fusion methods. We investigate the improved accuracy afforded by two different models of continuous-time preintegration and scenarios in which they exhibit superior performance. We further develop both indirect and direct graph-based VINS and demonstrate their competitive performance to state-of-the-art methods.

III. ESTIMATION PRELIMINARIES

The IMU state of an aided inertial navigation system at time step k is given by (Mourikis and Roumeliotis, 2007):

$$\mathbf{x}_k = [\mathbf{q}_k^\top \quad \mathbf{b}_{\omega_k}^\top \quad \mathbf{b}_{a_k}^\top \quad \mathbf{p}_k^\top]^\top \quad (1)$$

where \mathbf{q}_k is the unit quaternion of JPL form parameterizing the rotation \mathbf{R}_k from the global frame $\{G\}$ to the current local frame $\{k\}$ (Trawny and Roumeliotis, 2005), \mathbf{b}_{ω_k} and \mathbf{b}_{a_k} are the gyroscope and accelerometer biases, and \mathbf{p}_k are the velocity and position of the IMU expressed in the global frame, respectively.

We note that while the state is embedded in \mathbb{R}^{16} , there are actually 15 degrees of freedom (DOF), due to the constraint that \mathbf{q}_k must have unit length. In fact, the state lies on the manifold defined as the product of the unit quaternions with \mathbb{R}^{12} (i.e., $\mathcal{M}_{\mathbb{H}} \times \mathbb{R}^{12}$). In order to represent the estimation

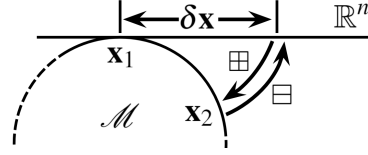


Fig. 1: Illustration of the state update operations on a manifold. The \boxplus operation maps $\mathbf{x}_1 \in \mathcal{M}$ and a vector $\delta \mathbf{x} \in \mathbb{R}^n$ to a new element $\mathbf{x}_2 \in \mathcal{M}$, while the \boxminus operation maps \mathbf{x}_1 and \mathbf{x}_2 to the vector $\delta \mathbf{x}$.

problem on manifold, we employ the “boxplus” update operation, \boxplus , which maps an element from a manifold, $\mathbf{x} \in \mathcal{M}$, and an error vector $\delta \mathbf{x}$ into a new element on \mathcal{M} (Hertzberg, Wagner, Frese, and Schröder, 2013). As illustrated in Figure 1, for a manifold of dimension n , we can define the following operation:

$$\boxplus : \mathcal{M} \times \mathbb{R}^n \rightarrow \mathcal{M} \quad (2)$$

$$\mathbf{x}_1 \boxplus \delta \mathbf{x} = \mathbf{x}_2 \quad (3)$$

Similarly, the inverse “boxminus” operation \boxminus is given by:

$$\boxminus : \mathcal{M} \times \mathcal{M} \rightarrow \mathbb{R}^n \quad (4)$$

$$\mathbf{x}_2 \boxminus \mathbf{x}_1 = \delta \mathbf{x} \quad (5)$$

In the case of a state in a vector space, $\mathbf{v} \in \mathbb{R}^n$, these operations are the standard addition and subtraction:

$$\mathbf{v}_1 \boxplus \delta \mathbf{v} \triangleq \mathbf{v}_1 + \delta \mathbf{v} = \mathbf{v}_2 \quad (6)$$

$$\mathbf{v}_2 \boxminus \mathbf{v}_1 \triangleq \mathbf{v}_2 - \mathbf{v}_1 = \delta \mathbf{v} \quad (7)$$

In the case of a unit quaternion expressed using the JPL convention, \bar{q} , we have (Trawny and Roumeliotis, 2005):

$$\bar{q}_1 \boxplus \delta \boldsymbol{\theta} \triangleq \begin{bmatrix} \frac{\delta \boldsymbol{\theta}}{2} \\ 1 \end{bmatrix} \otimes \bar{q}_1 = \bar{q}_2 \quad (8)$$

$$\bar{q}_2 \boxminus \bar{q}_1 \triangleq 2 \text{vec}(\bar{q}_2 \otimes \bar{q}_1^{-1}) = \delta \boldsymbol{\theta} \quad (9)$$

where $\text{vec}(\bar{q})$ refers to the vector portion of the quaternion argument (i.e., $\text{vec}([\mathbf{q}^\top q_4]^\top) = \mathbf{q}$). The quaternion multiplication, \otimes , is given by:

$$\bar{q} \otimes \bar{p} \triangleq \mathcal{R}(\bar{p}) \bar{q} = \mathcal{L}(\bar{q}) \bar{p} \quad (10)$$

$$\mathcal{R}(\bar{q}) = \begin{bmatrix} q_4 \mathbf{I} + [\mathbf{q}] & \mathbf{q} \\ -\mathbf{q}^\top & q_4 \end{bmatrix} \quad (11)$$

$$\mathcal{L}(\bar{p}) = \begin{bmatrix} p_4 \mathbf{I} - [\mathbf{p}] & \mathbf{p} \\ -\mathbf{p}^\top & p_4 \end{bmatrix} \quad (12)$$

where for $\mathbf{q} = [q_x \ q_y \ q_z]^\top$:

$$[\mathbf{q}] = \begin{bmatrix} 0 & -q_z & q_y \\ q_z & 0 & -q_x \\ -q_y & q_x & 0 \end{bmatrix} \quad (13)$$

In state estimation, these operations allow us to model the state on manifold using a Gaussian distribution on its *error state* vector. In particular, the random variable \mathbf{x} with mean value $\hat{\mathbf{x}}$ takes the form:

$$\mathbf{x} = \hat{\mathbf{x}} \boxplus \delta \mathbf{x} \quad (14)$$

$$\delta \mathbf{x} \sim \mathcal{N}(\mathbf{0}, \boldsymbol{\Sigma}) \quad (15)$$

where Σ is the covariance of the zero-mean error state. The error state corresponding to Equation (1) is given by:

$$\delta \mathbf{x}_k = [\delta \boldsymbol{\theta}_G^\top \quad \delta \mathbf{b}_{w_k}^\top \quad G \delta \mathbf{v}_k^\top \quad \delta \mathbf{b}_{a_k}^\top \quad G \delta \mathbf{p}_k^\top]^\top \quad (16)$$

A. Batch Optimization

In the case of graph SLAM, the graph nodes can correspond to historical robot states and features in the environment, while the edges represent collected measurements from sensors which relate the incident nodes. As an example, a robot measuring a feature would add an edge between the feature and the robot state node. Using this graph formulation and under the assumption of independent zero-mean Gaussian noise, we can find a maximum a posteriori (MAP) estimate of all states by solving the following nonlinear least-squares problem (Kummerle, Grisetti, Strasdat, Konolige, and Burgard, 2011):

$$\hat{\mathbf{x}} = \underset{\mathbf{x}}{\operatorname{argmin}} \sum_i \frac{1}{2} \|\mathbf{e}_i(\mathbf{x})\|_{\Lambda_i}^2 \quad (17)$$

where \mathbf{e}_i is the error/residual of measurement i , Λ_i is the associated information matrix (inverse covariance), and $\|\mathbf{v}\|_{\Lambda}^2 = \mathbf{v}^\top \Lambda \mathbf{v}$ represents the squared energy norm. Optimization is typically performed iteratively by linearizing the nonlinear measurements about the current estimate, $\hat{\mathbf{x}}$, and defining a new linear weighted least squares problem in terms of the error state $\delta \mathbf{x}$:

$$\delta \hat{\mathbf{x}} = \underset{\delta \mathbf{x}}{\operatorname{argmin}} \sum_i \frac{1}{2} \|\mathbf{e}_i(\hat{\mathbf{x}}) + \mathbf{J}_i \delta \mathbf{x}\|_{\Lambda_i}^2 \quad (18)$$

$$\mathbf{J}_i = \left. \frac{\partial \mathbf{e}_i(\hat{\mathbf{x}} \boxplus \delta \mathbf{x})}{\partial \delta \mathbf{x}} \right|_{\delta \mathbf{x}=\mathbf{0}} \quad (19)$$

We can see that the original optimization problem has been converted into finding the optimal *correction* vector, $\delta \mathbf{x}$, to the current state estimate. The optimal solution can be found by solving the following normal equation:

$$\left(\sum_i \mathbf{J}_i^\top \Lambda_i \mathbf{J}_i \right) \delta \hat{\mathbf{x}} = - \sum_i \mathbf{J}_i^\top \Lambda_i \mathbf{e}_i(\hat{\mathbf{x}}) \quad (20)$$

After obtaining the optimal correction, $\delta \hat{\mathbf{x}}$, we update our current estimate, $\hat{\mathbf{x}}^+ = \hat{\mathbf{x}} \boxplus \delta \hat{\mathbf{x}}$, and repeat the optimization process. After convergence, we will be left with the following distribution:

$$\mathbf{x} = \hat{\mathbf{x}} \boxplus \delta \mathbf{x} \quad (21)$$

$$\delta \mathbf{x} \sim \mathcal{N}(\mathbf{0}, \Sigma) \quad (22)$$

$$\Sigma = \left(\sum_i \mathbf{J}_i^\top \Lambda_i \mathbf{J}_i \right)^{-1} \quad (23)$$

where the measurement Jacobians, \mathbf{J}_i , are evaluated at the final estimate.

B. Marginalization

In a naive graph SLAM formulation, nodes are continuously added to the graph as time progresses without consideration to the computational burden. For example, as a robot moves through an unknown environment we would add robot state

nodes at *every* measurement time. This becomes a problem due to the high computational complexity, $O(n^3)$, of batch optimization, in the worst case. In order to bound the computational complexity of the system, marginalization is often performed to remove a set of nodes, called marginal states, from the graph, while retaining the information contained in their incident edges (see Figure 2 for an example) (Huang, Kaess, and Leonard, 2013; Eickenhoff, Paull, and Huang, 2016b). Partitioning the optimization variables into states remaining after marginalization, \mathbf{x}_r , and the to-be marginalized states, \mathbf{x}_m , we can write Equation (17) as the solution of the following minimization (Huang, Mourikis, and Roumeliotis, 2011):

$$\{\hat{\mathbf{x}}_r, \hat{\mathbf{x}}_m\} = \underset{\mathbf{x}_r, \mathbf{x}_m}{\operatorname{argmin}} \left(c_r(\mathbf{x}_r) + c_m(\mathbf{x}_m, \mathbf{x}_r) \right) \quad (24)$$

The second subcost, $c_m(\mathbf{x}_m, \mathbf{x}_r)$, is associated with the measurements incident to the marginal states, and is a function of both these states and the remaining ones. The first, $c_r(\mathbf{x}_r)$, refers to all other edges in the graph. The optimal estimate for the remaining nodes can be written as:

$$\hat{\mathbf{x}}_r = \underset{\mathbf{x}_r}{\operatorname{argmin}} \left(c_r(\mathbf{x}_r) + \min_{\mathbf{x}_m} c_m(\mathbf{x}_m, \mathbf{x}_r) \right) \quad (25)$$

That is, minimizing $c_m(\mathbf{x}_m, \mathbf{x}_r)$ with respect to \mathbf{x}_m yields a cost that is a function *only* of the remaining states. This minimization is performed as in Equation (20), where we write out the linear system for only the measurements involved in c_m :

$$\begin{bmatrix} \Lambda_{rr} & \Lambda_{rm} \\ \Lambda_{mr} & \Lambda_{mm} \end{bmatrix} \begin{bmatrix} \delta \mathbf{x}_r \\ \delta \mathbf{x}_m \end{bmatrix} = \begin{bmatrix} -\mathbf{g}_r \\ -\mathbf{g}_m \end{bmatrix} \quad (26)$$

The optimal subcost c_m , up to an irrelevant constant, is given by (Nerurkar, Wu, and Roumeliotis, 2014):²

$$c_{\text{marg}}(\mathbf{x}_r) = \frac{1}{2} \|\mathbf{x}_r \boxminus \check{\mathbf{x}}_r\|_{\Lambda_{\text{marg}}}^2 + \mathbf{g}_{\text{marg}}^\top (\mathbf{x}_r \boxminus \check{\mathbf{x}}_r) \quad (27)$$

where $\check{\mathbf{x}}_r$ is the linearization point used to build the system (in practice, the current state estimate at the time of marginalization), and $\Lambda_{\text{marg}} = \Lambda_{rr} - \Lambda_{rm} \Lambda_{mm}^{-1} \Lambda_{mr}$ and $\mathbf{g}_{\text{marg}} = \mathbf{g}_r - \Lambda_{rm} \Lambda_{mm}^{-1} \mathbf{g}_m$ are the marginalized Hessian and gradient, respectively.

In future optimization, this marginalization creates both a new quadratic *and* linear cost in terms of the error between the remaining states and their linearization points. This then replaces the marginal measurements in the original graph, and we can write this new cost up to a constant in the form of Equation (17):

$$c_{\text{marg}}(\mathbf{x}_r) = \frac{1}{2} \|\mathbf{A}_m(\mathbf{x}_r \boxminus \check{\mathbf{x}}_r) + \mathbf{b}_m\|_2^2 \quad (28)$$

$$\mathbf{A}_m^\top \mathbf{A}_m = \Lambda_{\text{marg}} \quad (29)$$

$$\mathbf{A}_m^\top \mathbf{b}_m = \mathbf{g}_{\text{marg}} \quad (30)$$

²Throughout the paper, we reserve the symbol \hat{x} to denote the current estimate of state variable x in optimization, while \check{x} refers to the (inferred) measurement mean value.

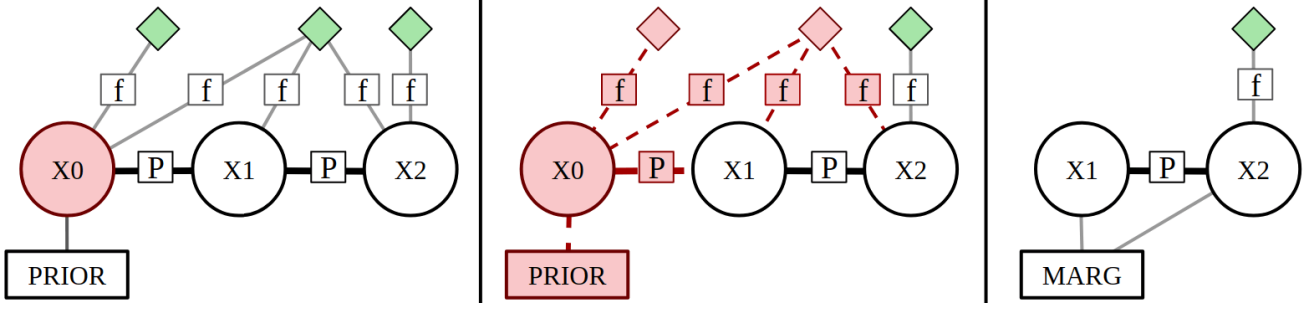


Fig. 2: During graph optimization of VINS, IMU states (shown in circles) and 3D features (diamonds) are included in the graph. Image projection measurements connect features and the IMU state corresponding to the time that the image was recorded. Subsequent IMU states are connected with preintegrated factors, while a prior factor connects to the oldest IMU state. During marginalization, we first select the states to be marginalized, e.g., the oldest IMU state in the window and its associated features (in red). With these measurements we perform marginalization to form a new marginal measurement for future optimization.

This cost yields the following residual and Jacobian for use in optimization (see Equations (18) and (19)):

$$\mathbf{e}_{\text{marg}}(\hat{\mathbf{x}}) = \mathbf{A}_m(\hat{\mathbf{x}}_r \boxminus \check{\mathbf{x}}_r) + \mathbf{b}_m \quad (31)$$

$$\mathbf{J}_{\text{marg}} = \mathbf{A}_m \frac{\partial((\hat{\mathbf{x}}_r \boxminus \delta \mathbf{x}_r) \boxminus \check{\mathbf{x}}_r)}{\partial \delta \mathbf{x}_r} \Big|_{\delta \mathbf{x}_r = \mathbf{0}} \quad (32)$$

where for the Jacobian of a vector (i.e., if $\mathbf{x}_r = \mathbf{v}$):

$$\frac{\partial((\hat{\mathbf{v}} \boxminus \delta \mathbf{v}) \boxminus \check{\mathbf{v}})}{\partial \delta \mathbf{v}} = \frac{\partial(\hat{\mathbf{v}} + \delta \mathbf{v} - \check{\mathbf{v}})}{\partial \delta \mathbf{v}} = \mathbf{I} \quad (33)$$

and for a quaternion \tilde{q} , with $\tilde{q} = \hat{q} \otimes \check{q}^{-1}$, we have:

$$\begin{aligned} \frac{\partial((\hat{q} \boxminus \delta \theta) \boxminus \check{q})}{\partial \delta \theta} &= \frac{\partial 2\text{vec}\left(\left[\begin{smallmatrix} \delta \theta \\ 2 \\ 1 \end{smallmatrix}\right] \otimes \hat{q} \otimes \check{q}^{-1}\right)}{\partial \delta \theta} \\ &= \frac{\partial 2\text{vec}\left(\mathcal{R}(\tilde{q}) \left[\begin{smallmatrix} \delta \theta \\ 2 \\ 1 \end{smallmatrix}\right]\right)}{\partial \delta \theta} \\ &= \tilde{q}_4 \mathbf{I} + [\tilde{\mathbf{q}}] \end{aligned} \quad (34)$$

IV. CONTINUOUS PREINTEGRATION

In this section, we present in detail the proposed continuous IMU preintegration based on two different realistic inertial models, which is expected to be readily used in any graph-based aided inertial navigation, thus providing an essential building block for visual-inertial state estimation.

An IMU attached to the robot collects inertial readings of the underlying state dynamics. In particular, the sensor receives angular velocity ω_m and local linear acceleration \mathbf{a}_m measurements which relate to the corresponding true values ω and \mathbf{a} as follows:

$$\omega_m = \omega + \mathbf{b}_\omega + \mathbf{n}_\omega \quad (35)$$

$$\mathbf{a}_m = \mathbf{a} + {}^I_G \mathbf{R}^G \mathbf{g} + \mathbf{b}_a + \mathbf{n}_a \quad (36)$$

where ${}^G \mathbf{g} = [0 \ 0 \ 9.81]^\top$ is the global gravity³ and ${}^I_G \mathbf{R}$ is the rotation from the global frame to the instantaneous local inertial frame. The measurements are corrupted both by the time-varying biases \mathbf{b}_ω and \mathbf{b}_a (which must be co-estimated with the state), and the zero-mean white Gaussian noises \mathbf{n}_ω

and \mathbf{n}_a . The standard dynamics of the IMU state is given by (Chatfield, 1997):

$${}^I_G \dot{\bar{q}} = \frac{1}{2} \Omega(\omega_m - \mathbf{b}_\omega - \mathbf{n}_\omega) {}^I_G \bar{q} \quad (37)$$

$$\dot{\mathbf{b}}_\omega = \mathbf{n}_{\omega b} \quad (38)$$

$${}^G \dot{\mathbf{v}}_I = {}^G \mathbf{R}(\mathbf{a}_m - \mathbf{b}_a - \mathbf{n}_a) - {}^G \mathbf{g} \quad (39)$$

$$\dot{\mathbf{b}}_a = \mathbf{n}_{ab} \quad (40)$$

$${}^G \dot{\mathbf{p}}_I = {}^G \mathbf{v}_I \quad (41)$$

where

$$\Omega(\omega) = \begin{bmatrix} -[\omega] & \omega \\ \omega^\top & 0 \end{bmatrix} \quad (42)$$

A. Standard IMU Processing

Given a series of IMU measurements, \mathcal{I} , collected over a time interval $[t_k, t_{k+1}]$, the standard (graph-based) IMU processing considers the following propagation function:

$$\mathbf{x}_{k+1} = \mathbf{g}(\mathbf{x}_k, \mathcal{I}, \mathbf{n}) \quad (43)$$

That is, the future state at time step $k+1$ is a function of the current state at step k , the IMU measurements \mathcal{I} , and the corresponding measurement noise \mathbf{n} . Conditioning on the current state, the expected value of the next state is found by evaluating the propagation function with zero noise:

$$\check{\mathbf{x}}_{k+1} = \mathbf{g}(\mathbf{x}_k, \mathcal{I}, \mathbf{0}) \quad (44)$$

which implies that we perform integration of the state dynamics in the absence of noise. The residual for use in batch optimization of this propagation now constrains the start and end states of the interval and is given by (see Equation (17)):

$$c_{IMU}(\mathbf{x}) = \frac{1}{2} \|\mathbf{x}_{k+1} \boxminus \check{\mathbf{x}}_{k+1}\|_{\mathbf{Q}_k}^2 \quad (45)$$

$$= \frac{1}{2} \|\mathbf{x}_{k+1} \boxminus \mathbf{g}(\mathbf{x}_k, \mathcal{I}, \mathbf{0})\|_{\mathbf{Q}_k}^2 \quad (46)$$

where \mathbf{Q}_k is the linearized, discrete-time noise covariance computed from the IMU noise characterization and is a *function of the state*. This noise covariance matrix and the propagation function can be found by the integration of Equations (37)-(41) and their associated error state dynamics,

³Note that the gravity is slightly different in different parts of the globe.

to which we refer the reader to (Trawny and Roumeliotis, 2005; Mourikis and Roumeliotis, 2007). It is clear from Equation (44) that we need constantly re-evaluate the propagation function $\mathbf{g}(\cdot)$ and the residual covariance \mathbf{Q}_k whenever the linearization point (state estimate) changes. The high frequency nature of the IMU sensors and the complexity of the propagation function and the noise covariance can make direct incorporation of IMU data in real-time graph-based SLAM prohibitively expensive.

B. Model 1: Piecewise Constant Measurements

IMU preintegration seeks to directly reduce the computational complexity of incorporating inertial measurements by removing the need to re-integrate the propagation function and noise covariance. This is achieved by processing IMU measurements in a *local* frame of reference, yielding measurements that are, in contrast to Equation (44), independent of the state (Lupton and Sukkarieh, 2012).

Specifically, by denoting $\Delta T = t_{k+1} - t_k$, we have the following relationship between a series of IMU measurements, the start state, and the resulting end state (Eckenhoff, Geneva, and Huang, 2016a):

$$\begin{aligned} {}^G\mathbf{p}_{k+1} &= {}^G\mathbf{p}_k + {}^G\mathbf{v}_k\Delta T - \frac{1}{2}{}^G\mathbf{g}\Delta T^2 \\ &\quad + {}^G\mathbf{R} \int_{t_k}^{t_{k+1}} \int_{t_k}^s {}^k\mathbf{R}(\mathbf{a}_m - \mathbf{b}_a - \mathbf{n}_a) du ds \end{aligned} \quad (47)$$

$$\begin{aligned} {}^G\mathbf{v}_{k+1} &= {}^G\mathbf{v}_k - {}^G\mathbf{g}\Delta T \\ &\quad + {}^G\mathbf{R} \int_{t_k}^{t_{k+1}} {}^k\mathbf{R}(\mathbf{a}_m - \mathbf{b}_a - \mathbf{n}_a) du \end{aligned} \quad (48)$$

$${}^{k+1}\mathbf{R} = {}^k\mathbf{R} {}^k\mathbf{R}_G \quad (49)$$

$$\mathbf{b}_{\omega_{k+1}} = \mathbf{b}_{\omega_k} + \int_{t_k}^{t_{k+1}} \mathbf{n}_{\omega b} du \quad (50)$$

$$\mathbf{b}_{a_{k+1}} = \mathbf{b}_{a_k} + \int_{t_k}^{t_{k+1}} \mathbf{n}_{ab} du \quad (51)$$

From the above, we define the following preintegrated IMU measurements:⁴

$${}^k\boldsymbol{\alpha}_{k+1} = \int_{t_k}^{t_{k+1}} \int_{t_k}^s {}^k\mathbf{R}(\mathbf{a}_m - \mathbf{b}_a - \mathbf{n}_a) du ds \quad (52)$$

$${}^k\boldsymbol{\beta}_{k+1} = \int_{t_k}^{t_{k+1}} {}^k\mathbf{R}(\mathbf{a}_m - \mathbf{b}_a - \mathbf{n}_a) du \quad (53)$$

To remove the dependencies of the above preintegrated measurements on the true biases, we linearize about the

⁴ Note that along with the preintegrated inertial measurements in Equations (52) and (53), the preintegrated relative-orientation measurement ${}^{k+1}\tilde{\mathbf{q}}$ (or ${}^{k+1}\mathbf{R}$) can be obtained from the integration of the gyro measurements.

current bias estimates at time step t_k , $\mathbf{b}_{a_k}^*$ and $\mathbf{b}_{\omega_k}^*$. Defining $\Delta\mathbf{b} = \mathbf{b} - \mathbf{b}^*$, we have:

$${}^k\mathbf{R} \left({}^G\mathbf{p}_{k+1} - {}^G\mathbf{p}_k - {}^G\mathbf{v}_k\Delta T + \frac{1}{2}{}^G\mathbf{g}\Delta T^2 \right) \simeq \quad (54)$$

$$\begin{aligned} &{}^k\boldsymbol{\alpha}_{k+1}(\mathbf{b}_{\omega_k}^*, \mathbf{b}_{a_k}^*) + \frac{\partial \boldsymbol{\alpha}}{\partial \mathbf{b}_{\omega}} \Big|_{\mathbf{b}_{\omega_k}^*} \Delta \mathbf{b}_{\omega} + \frac{\partial \boldsymbol{\alpha}}{\partial \mathbf{b}_a} \Big|_{\mathbf{b}_{a_k}^*} \Delta \mathbf{b}_a \\ &{}^k\mathbf{R} ({}^G\mathbf{v}_{k+1} - {}^G\mathbf{v}_k + {}^G\mathbf{g}\Delta T) \simeq \end{aligned} \quad (55)$$

$$\begin{aligned} &{}^k\boldsymbol{\beta}_{k+1}(\mathbf{b}_{\omega_k}^*, \mathbf{b}_{a_k}^*) + \frac{\partial \boldsymbol{\beta}}{\partial \mathbf{b}_{\omega}} \Big|_{\mathbf{b}_{\omega_k}^*} \Delta \mathbf{b}_{\omega} + \frac{\partial \boldsymbol{\beta}}{\partial \mathbf{b}_a} \Big|_{\mathbf{b}_{a_k}^*} \Delta \mathbf{b}_a \\ &{}^{k+1}\mathbf{R} {}^k\mathbf{R}^\top \simeq \mathbf{R} \left(\frac{\partial \mathbf{R}}{\partial \mathbf{b}_{\omega}} \Big|_{\mathbf{b}_{\omega_k}^*} \Delta \mathbf{b}_{\omega} \right) {}^k\mathbf{R}(\mathbf{b}_{\omega_k}^*) \end{aligned} \quad (56)$$

Note that Equations (54) and (55) are simple Taylor series expansions for our ${}^k\boldsymbol{\alpha}_{k+1}$ and ${}^k\boldsymbol{\beta}_{k+1}$ measurements, while Equation (56) models an additional rotation induced due to a change of the linearization point (estimate) of the gyro bias (Forster, Carlone, Dellaert, and Scaramuzza, 2015; Eckenhoff, Geneva, and Huang, 2016a).

The preintegrated measurement's mean values, ${}^k\check{\boldsymbol{\alpha}}_{k+1}$, ${}^k\check{\boldsymbol{\beta}}_{k+1}$, and ${}^{k+1}\check{\mathbf{q}}$, must be computed for use in graph optimization. It is important to note that current preintegration methods (Lupton and Sukkarieh, 2012; Forster, Carlone, Dellaert, and Scaramuzza, 2015; Ling, Liu, and Shen, 2016) are all based on discrete integration of the measurement dynamics through Euler or midpoint integration. In particular, the discrete approximation used by Forster, Carlone, Dellaert, and Scaramuzza (2015) in fact corresponds to a piecewise constant *global acceleration* model. By contrast, we here offer *closed-form* solutions for the measurement means under the assumptions of piecewise constant *measurements* and of piecewise constant *local acceleration* (in Section IV-C).

1) *Computing preintegration mean:* Between two image times, t_k and t_{k+1} , the IMU receives a series of inertial measurements. We denote τ as the step at which an IMU measurement is received, and $\tau + 1$ as the step of the *next* IMU reading. The time associated with each of these steps is given by t_τ and $t_{\tau+1}$, respectively. The relative orientation between the interval, ${}^{k+1}\check{\mathbf{q}}$, can be found using successive applications of the zeroth order quaternion integrator (Trawny and Roumeliotis, 2005). Based on the definitions of ${}^k\boldsymbol{\alpha}_{k+1}$ and ${}^k\boldsymbol{\beta}_{k+1}$ (see Equations (52) and (53)), we have the following continuous-time dynamics at every step u with $t_u \in [t_\tau, t_{\tau+1}]$:

$${}^k\dot{\boldsymbol{\alpha}}_u = {}^k\boldsymbol{\beta}_u \quad (57)$$

$${}^k\dot{\boldsymbol{\beta}}_u = {}^k\mathbf{R}(\mathbf{a}_m - \mathbf{b}_a - \mathbf{n}_a) \quad (58)$$

From these governing differential equations, we formulate the following *linear* system that describes the evolution of the measurements by taking the expectation operation:

$$\begin{bmatrix} {}^k\dot{\boldsymbol{\alpha}}_u \\ {}^k\dot{\boldsymbol{\beta}}_u \end{bmatrix} = \begin{bmatrix} \mathbf{0} & \mathbf{I} \\ \mathbf{0} & \mathbf{0} \end{bmatrix} \begin{bmatrix} {}^k\check{\boldsymbol{\alpha}}_u \\ {}^k\check{\boldsymbol{\beta}}_u \end{bmatrix} + \begin{bmatrix} \mathbf{0} \\ {}^k\check{\mathbf{R}} \end{bmatrix} (\mathbf{a}_m - \mathbf{b}_{a_k}^*) \quad (59)$$

Given \mathbf{a}_m and $\boldsymbol{\omega}_m$ sampled at time t_τ and assuming that these IMU measurements are *piecewise constant* during $[t_\tau, t_{\tau+1}]$, we analytically solve the above linear time-varying

(LTV) system to obtain the updated preintegration mean values, which are computed as follows

$$\begin{bmatrix} {}^k\check{\alpha}_{\tau+1} \\ {}^k\check{\beta}_{\tau+1} \end{bmatrix} = \begin{bmatrix} {}^k\check{\alpha}_{\tau} + {}^k\check{\beta}_{\tau}\Delta t \\ {}^k\check{\beta}_{\tau} \end{bmatrix} + \begin{bmatrix} {}^k\check{\mathbf{R}}_{\tau+1}(\frac{\Delta t^2}{2}\mathbf{I}_{3\times 3} + \frac{|\dot{\omega}|\Delta t\cos(|\dot{\omega}|\Delta t) - \sin(|\dot{\omega}|\Delta t)}{|\dot{\omega}|^3}[\dot{\omega}]) \\ + \frac{(|\dot{\omega}|\Delta t)^2 - 2\cos(|\dot{\omega}|\Delta t) - 2(|\dot{\omega}|\Delta t)\sin(|\dot{\omega}|\Delta t) + 2}{2|\dot{\omega}|^4}[\dot{\omega}]^2)(\hat{\mathbf{a}}) \\ \hline {}^k\check{\mathbf{R}}_{\tau+1}(\Delta t\mathbf{I}_{3\times 3} - \frac{1 - \cos(|\dot{\omega}|\Delta t)}{|\dot{\omega}|^2}[\dot{\omega}]) \\ + \frac{(|\dot{\omega}|\Delta t) - \sin(|\dot{\omega}|\Delta t)}{|\dot{\omega}|^3}[\dot{\omega}]^2)(\hat{\mathbf{a}}) \end{bmatrix} \quad (60)$$

where we have employed the definitions: $\hat{\omega} = \omega_m - \mathbf{b}_{\omega_k}^*$, $\hat{\mathbf{a}} = \mathbf{a}_m - \mathbf{b}_{a_k}^*$, and $\Delta t = t_{\tau+1} - t_{\tau}$. Clearly, these *closed-form* expressions reveal the higher order affect of the angular velocity on the preintegrated measurements due to the evolution of the orientation over the IMU sampling interval.

2) *Computing preintegration covariance*: In order to derive the preintegrated measurement covariance, we first write the linearized *measurement* error state system as follows (Eckenhoff et al., 2018):

$$\begin{bmatrix} {}^u\delta\theta_k \\ \tilde{\mathbf{b}}_{\omega} \\ {}^k\delta\beta_u \\ \tilde{\mathbf{b}}_a \\ {}^k\delta\alpha_u \end{bmatrix} = \begin{bmatrix} -[\dot{\omega}] & -\mathbf{I} & \mathbf{0} & \mathbf{0} & \mathbf{0} \\ \mathbf{0} & \mathbf{0} & \mathbf{0} & \mathbf{0} & \mathbf{0} \\ -{}^k\check{\mathbf{R}}_u[\hat{\mathbf{a}}] & \mathbf{0} & \mathbf{0} & -{}^k\check{\mathbf{R}} & \mathbf{0} \\ \mathbf{0} & \mathbf{0} & \mathbf{0} & \mathbf{0} & \mathbf{0} \\ \mathbf{0} & \mathbf{0} & \mathbf{I} & \mathbf{0} & \mathbf{0} \end{bmatrix} \begin{bmatrix} {}^u\delta\theta_k \\ \tilde{\mathbf{b}}_{\omega} \\ {}^k\delta\beta_u \\ \tilde{\mathbf{b}}_a \\ {}^k\delta\alpha_u \end{bmatrix} + \begin{bmatrix} -\mathbf{I} & \mathbf{0} & \mathbf{0} & \mathbf{0} \\ \mathbf{0} & \mathbf{I} & \mathbf{0} & \mathbf{0} \\ \mathbf{0} & \mathbf{0} & -{}^k\check{\mathbf{R}} & \mathbf{0} \\ \mathbf{0} & \mathbf{0} & \mathbf{0} & \mathbf{I} \\ \mathbf{0} & \mathbf{0} & \mathbf{0} & \mathbf{0} \end{bmatrix} \begin{bmatrix} \mathbf{n}_{\omega} \\ \mathbf{n}_{\omega b} \\ \mathbf{n}_a \\ \mathbf{n}_{ab} \end{bmatrix} \quad (61)$$

$$\Rightarrow \dot{\mathbf{r}} = \mathbf{F}\mathbf{r} + \mathbf{G}\mathbf{n} \quad (62)$$

which is akin to the standard VINS error state propagation equations in a local frame of reference (Mourikis and Roumeliotis, 2007).

It is important to note that in contrast to our previous work (Eckenhoff et al., 2016a, 2017), we here couple the preintegration bias and measurement evolution for improved accuracy. Note also that the bias error terms in Equation (61), $\tilde{\mathbf{b}}_{\omega}$ and $\tilde{\mathbf{b}}_a$, describe the deviation of the bias over the interval due to the random-walk drift, rather than the error of the current bias estimate. Covariance propagation can be carried out using integration to obtain the discrete state transition matrix $\Phi(t_{\tau+1}, t_{\tau})$:

$$\dot{\Phi}(t_u, t_{\tau}) = \mathbf{F}(u) \Phi(t_u, t_{\tau}) \quad (63)$$

$$\Phi(t_{\tau}, t_{\tau}) = \mathbf{I}_{15\times 15} \quad (64)$$

The propagation of the measurement covariance, \mathbf{P} , takes the following form:

$$\mathbf{P}_k = \mathbf{0}_{15\times 15} \quad (65)$$

$$\mathbf{P}_{\tau+1} = \Phi(t_{\tau+1}, t_{\tau}) \mathbf{P}_{\tau} \Phi(t_{\tau+1}, t_{\tau})^{\top} + \mathbf{Q}_{\tau} \quad (66)$$

$$\mathbf{Q}_{\tau} = \int_{t_{\tau}}^{t_{\tau+1}} \Phi(t_{\tau+1}, u) \mathbf{G}(u) \mathbf{Q}_c \mathbf{G}(u)^{\top} \Phi(t_{\tau+1}, u)^{\top} du \quad (67)$$

where \mathbf{Q}_c is the continuous-time IMU noise covariance. To keep presentation concise, the discrete-time noise covariance \mathbf{Q}_{τ} can be computed similarly as in (Trawny and Roumeliotis, 2005).

3) Preintegration measurement residuals and Jacobians:

For use in optimization, we form the associated measurement cost and residual as follows:

$$c_{IMU}(\mathbf{x}) = \frac{1}{2} \|\mathbf{e}_{IMU}(\mathbf{x})\|_{\mathbf{P}_{k+1}^{-1}}^2 \quad (68)$$

$$\mathbf{e}_{IMU}(\mathbf{x}) = \quad (69)$$

$$\begin{bmatrix} 2\text{vec}({}^{k+1}_G\bar{q} \otimes {}^k_G\bar{q}^{-1} \otimes {}^{k+1}_G\bar{q}^{-1} \otimes \bar{q}_b) \\ \hline \mathbf{b}_{\omega_{k+1}} - \mathbf{b}_{\omega_k} \\ \hline \left({}^k_G\mathbf{R}({}^G\mathbf{v}_{k+1} - {}^G\mathbf{v}_k + {}^G\mathbf{g}\Delta t) \right. \\ \left. - \mathbf{J}_{\beta}(\mathbf{b}_{\omega_k} - \mathbf{b}_{\omega_k}^*) - \mathbf{H}_{\beta}(\mathbf{b}_{a_k} - \mathbf{b}_{a_k}^*) - {}^k\check{\beta}_{k+1} \right) \\ \hline \mathbf{b}_{a_{k+1}} - \mathbf{b}_{a_k} \\ \hline \left({}^k_G\mathbf{R}({}^G\mathbf{p}_{k+1} - {}^G\mathbf{p}_k - {}^G\mathbf{v}_k\Delta t + \frac{1}{2}{}^G\mathbf{g}\Delta t^2) \right. \\ \left. - \mathbf{J}_{\alpha}(\mathbf{b}_{\omega_k} - \mathbf{b}_{\omega_k}^*) - \mathbf{H}_{\alpha}(\mathbf{b}_{a_k} - \mathbf{b}_{a_k}^*) - {}^k\check{\alpha}_{k+1} \right) \end{bmatrix}$$

where we have employed $\bar{q}_b = \begin{bmatrix} \frac{\theta}{\|\theta\|} \sin\left(\frac{\|\theta\|}{2}\right) \\ \cos\left(\frac{\|\theta\|}{2}\right) \end{bmatrix}$ and $\theta =$

$\mathbf{J}_q(\mathbf{b}_{\omega_k} - \mathbf{b}_{\omega_k}^*)$. In the above expression, \mathbf{J}_q , \mathbf{J}_{α} , \mathbf{J}_{β} , \mathbf{H}_{α} , and \mathbf{H}_{β} , are the Jacobian matrices of the pertinent residuals with respect to the biases, which are used to correct the measurements due to a change in the initial bias estimate \mathbf{b}^* , thus compensating for the fact that preintegrated measurements have been linearized about $\mathbf{b}_{\omega_k}^*$ and $\mathbf{b}_{a_k}^*$ without having to recompute the required integrals whenever the bias estimates change. In particular, using the fact that our preintegrated measurement means are linear in the acceleration bias \mathbf{b}_a (see Equation (60)), we have the following dynamics of its Jacobians:

$$\begin{bmatrix} \frac{\partial \alpha}{\partial \mathbf{b}_a} \\ \frac{\partial \beta}{\partial \mathbf{b}_a} \end{bmatrix} =: \begin{bmatrix} \mathbf{H}_{\alpha}(\tau+1) \\ \mathbf{H}_{\beta}(\tau+1) \end{bmatrix} = \begin{bmatrix} \mathbf{H}_{\alpha}(\tau) + \mathbf{H}_{\beta}(\tau)\Delta t \\ \mathbf{H}_{\beta}(\tau) \end{bmatrix} - \begin{bmatrix} {}^k\check{\mathbf{R}}_{\tau+1}(\frac{\Delta t^2}{2}\mathbf{I}_{3\times 3} + \frac{|\dot{\omega}|\Delta t\cos(|\dot{\omega}|\Delta t) - \sin(|\dot{\omega}|\Delta t)}{|\dot{\omega}|^3}[\dot{\omega}]) \\ + \frac{(|\dot{\omega}|\Delta t)^2 - 2\cos(|\dot{\omega}|\Delta t) - 2(|\dot{\omega}|\Delta t)\sin(|\dot{\omega}|\Delta t) + 2}{2|\dot{\omega}|^4}[\dot{\omega}]^2) \\ \hline {}^k\check{\mathbf{R}}_{\tau+1}(\Delta t\mathbf{I}_{3\times 3} - \frac{1 - \cos(|\dot{\omega}|\Delta t)}{|\dot{\omega}|^2}[\dot{\omega}]) \\ + \frac{(|\dot{\omega}|\Delta t) - \sin(|\dot{\omega}|\Delta t)}{|\dot{\omega}|^3}[\dot{\omega}]^2) \end{bmatrix}$$

Similarly, for the gyroscope bias Jacobians, we have:

$$\begin{bmatrix} \frac{\partial \alpha}{\partial \mathbf{b}_{\omega}} \\ \frac{\partial \beta}{\partial \mathbf{b}_{\omega}} \end{bmatrix} =: \begin{bmatrix} \mathbf{J}_{\alpha}(\tau+1) \\ \mathbf{J}_{\beta}(\tau+1) \end{bmatrix} = \begin{bmatrix} \mathbf{J}_{\alpha}(\tau) + \mathbf{J}_{\beta}(\tau)\Delta t \\ \mathbf{J}_{\beta}(\tau) \end{bmatrix} + \begin{bmatrix} \frac{\partial \mathbf{A}_{\tau}}{\partial \mathbf{b}_{\omega}} \\ \frac{\partial \mathbf{B}_{\tau}}{\partial \mathbf{b}_{\omega}} \end{bmatrix}$$

where \mathbf{A}_{τ} and \mathbf{B}_{τ} are the terms in the second matrix of Equation (60). Moreover, the measurement Jacobians of these preintegrated measurements with respect to the error state,

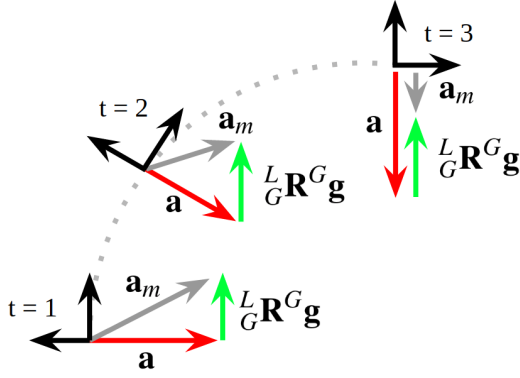


Fig. 3: An example of an IMU rotating against the gravity. It can be seen that the true local acceleration \mathbf{a} (red) remains constant, while the measurement \mathbf{a}_m (grey) changes continuously due to the effect of gravity (green).

Equation (16), can also be found in Appendix A.1, which are essential for the batch optimization solver. For the detailed derivations and closed-form expressions of the preintegrated measurements and Jacobians, the reader is referred to our companion technical report (Eckenhoff et al., 2018).

C. Model 2: Piecewise Constant Local Acceleration

The previous preintegration (Model 1) assumes that noiseless IMU measurements can be approximated as remaining constant over a sampling interval, which, however, might not always be a good approximation (see Figure 3). In this section, we propose a new preintegration model that instead assumes piecewise constant *true* local acceleration during the sampling time interval, which may better approximate motion dynamics in practice.

To this end, we first rewrite Equations (47) and (48) as:

$${}^G\mathbf{p}_{k+1} = {}^G\mathbf{p}_k + {}^G\mathbf{v}_k\Delta T + {}^G\mathbf{R} \int_{t_k}^{t_{k+1}} \int_{t_k}^s {}^k\mathbf{R}_u \mathbf{a} \, du \, ds \quad (70)$$

$${}^G\mathbf{v}_{k+1} = {}^G\mathbf{v}_k + {}^G\mathbf{R} \int_{t_k}^{t_{k+1}} {}^k\mathbf{R}_u \mathbf{a} \, du \quad (71)$$

Note that we have moved the effect of gravity back inside the integrals. We then define the following vectors:

$$\Delta p = \int_{t_k}^{t_{k+1}} \int_{t_k}^s {}^k\mathbf{R}_u \mathbf{a} \, du \, ds \quad (72)$$

$$\Delta v = \int_{t_k}^{t_{k+1}} {}^k\mathbf{R}_u \mathbf{a} \, du \quad (73)$$

which essentially are the true local position displacement and velocity change during $[t_k, t_{k+1}]$, and yields:

$$\Delta \dot{p} = \Delta v \quad (74)$$

$$\Delta \dot{v} = {}^k\mathbf{R}_u \mathbf{a} \quad (75)$$

In particular, between two IMU measurement times inside the preintegration interval, $[t_\tau, t_{\tau+1}] \subset [t_k, t_{k+1}]$, we assume that the *local* acceleration will be constant:

$$\forall t_u \in [t_\tau, t_{\tau+1}], \quad \mathbf{a}(t_u) = \mathbf{a}(t_\tau) \quad (76)$$

Using this sampling model we can rewrite Equation (75) as:

$$\Delta \dot{v} = {}^k\mathbf{R}_u (\mathbf{a}_m - \mathbf{b}_a - \mathbf{n}_a - {}^\tau\mathbf{R}_G^k \mathbf{R}^G \mathbf{g}) \quad (77)$$

We now write the relationship of the states at the beginning and end of the interval as (see Equations (70) and (71)):

$${}^k\mathbf{R} ({}^G\mathbf{p}_{k+1} - {}^G\mathbf{p}_k - {}^G\mathbf{v}_k\Delta T) = \Delta p \quad (78)$$

$${}^k\mathbf{R} ({}^G\mathbf{v}_{k+1} - {}^G\mathbf{v}_k) = \Delta v \quad (79)$$

It is important to note that, since Δp and Δv are functions of both the biases *and* the initial orientation, we perform the following linearization with respect to these states:

$$\begin{aligned} {}^k\mathbf{R} ({}^G\mathbf{p}_{k+1} - {}^G\mathbf{p}_k - {}^G\mathbf{v}_k\Delta T) &\simeq \Delta p (\mathbf{b}_{\omega_k}^*, \mathbf{b}_{a_k}^*, {}^k\bar{q}^*) \\ &+ \frac{\partial \Delta p}{\partial \mathbf{b}_{\omega}} \Big|_{\mathbf{b}_{\omega_k}^*} \Delta \mathbf{b}_{\omega} + \frac{\partial \Delta p}{\partial \mathbf{b}_a} \Big|_{\mathbf{b}_{a_k}^*} \Delta \mathbf{b}_a + \frac{\partial \Delta p}{\partial \Delta \theta_k} \Big|_{{}^k\bar{q}^*} \Delta \theta_k \end{aligned}$$

$$\begin{aligned} {}^k\mathbf{R} ({}^G\mathbf{v}_{k+1} - {}^G\mathbf{v}_k) &\simeq \Delta v (\mathbf{b}_{\omega_k}^*, \mathbf{b}_{a_k}^*, {}^k\bar{q}^*) \\ &+ \frac{\partial \Delta v}{\partial \mathbf{b}_{\omega}} \Big|_{\mathbf{b}_{\omega_k}^*} \Delta \mathbf{b}_{\omega} + \frac{\partial \Delta v}{\partial \mathbf{b}_a} \Big|_{\mathbf{b}_{a_k}^*} \Delta \mathbf{b}_a + \frac{\partial \Delta v}{\partial \Delta \theta_k} \Big|_{{}^k\bar{q}^*} \Delta \theta_k \end{aligned}$$

where $\Delta \theta_k = 2\text{vec}({}^k\bar{q} \otimes {}^k\bar{q}^{*-1})$ is the rotation angle change associated with the change of the linearization point of quaternion ${}^k\bar{q}$.

1) *Computing preintegration mean:* To compute the new preintegrated measurement mean values, we first determine the continuous-time dynamics of the expected preintegration vectors by taking expectations of Equations (74) and (77), given by:

$$\Delta \dot{p} = \Delta \check{v} \quad (80)$$

$$\Delta \dot{v} = {}^k\check{\mathbf{R}}_u (\mathbf{a}_m - \mathbf{b}_{a_k}^* - {}^\tau\check{\mathbf{R}}_G^k \mathbf{R}^G \mathbf{g}) \quad (81)$$

As in the case of Model 1 (see Section IV-B1), we can formulate a linear system of the new preintegration measurement vectors and find the closed-form solutions. Specifically, we can integrate these differential equations and obtain the solution similar to Equation (60), while using the new definition: $\hat{\mathbf{a}} = \mathbf{a}_m - \mathbf{b}_{a_k}^* - {}^\tau\check{\mathbf{R}}_G^k \mathbf{R}^G \mathbf{g}$, which serves as the estimate for the piecewise constant local acceleration over the sampling interval.

2) *Computing preintegration covariance:* To compute the new preintegration measurement covariance, we first determine the differential equations for the corresponding preintegration measurement errors (see Equations (74), (77), (80) and (81)):

$$\Delta \dot{\tilde{p}} = \Delta v - \Delta \check{v} = \Delta \tilde{v} \quad (82)$$

$$\begin{aligned} \Delta \dot{\tilde{v}} &= {}^k\check{\mathbf{R}}_u (\mathbf{I} + [{}^\tau\delta\theta_k]) (\mathbf{a}_m - \mathbf{b}_{a_k}^* - \tilde{\mathbf{b}}_a \\ &\quad - (\mathbf{I} - [{}^\tau\delta\theta_k]) {}^\tau\check{\mathbf{R}}_G^k (\mathbf{I} - [\Delta\theta_k]) {}^k\mathbf{R}^G \mathbf{g} - \mathbf{n}_a) \\ &\quad - {}^k\check{\mathbf{R}}_u (\mathbf{a}_m - \mathbf{b}_{a_k}^* - {}^\tau\check{\mathbf{R}}_G^k \mathbf{R}^G \mathbf{g}) \\ &= -{}^k\check{\mathbf{R}}_u [\hat{\mathbf{a}}]^u \delta\theta_k - {}^k\check{\mathbf{R}}_u \tilde{\mathbf{b}}_a \\ &\quad - {}^k\check{\mathbf{R}}_u [{}^\tau\check{\mathbf{g}}]^\tau \delta\theta_k - {}^k\check{\mathbf{R}}_u \check{\mathbf{R}}_G^k [\mathbf{g}^*]^\tau \Delta\theta_k - {}^k\check{\mathbf{R}}_u \mathbf{n}_a \end{aligned} \quad (83)$$

where ${}^k\mathbf{g}^* = {}^k\mathbf{R}^G \mathbf{g}$ is the global gravity rotated into the local frame of the linearization point. Similarly, ${}^\tau\check{\mathbf{g}}$ represents the estimate for gravity in the sampled τ frame. In the

above expressions, we have used three angle errors: (i) ${}^u\delta\theta_k$ corresponds to the active local IMU orientation error, (ii) ${}^\tau\delta\theta_k$ corresponds to the cloned orientation error at the sampling time t_τ , and (iii) $\Delta\theta_k$ is the *global* angle error of the starting orientation of the preintegration time interval. In addition, the bias errors $\tilde{\mathbf{b}}$ describe the deviation of the bias from the starting value over the interval due to bias drift. With this, we have the following time evolution of the full preintegrated measurement error state:

$$\begin{bmatrix} {}^u\delta\dot{\theta}_k \\ \dot{\tilde{\mathbf{b}}}_\omega \\ \Delta\dot{\tilde{v}} \\ \dot{\tilde{\mathbf{b}}}_a \\ \Delta\dot{\tilde{p}} \\ {}^\tau\delta\dot{\theta}_k \\ \Delta\dot{\theta}_k \end{bmatrix} = \mathbf{F} \begin{bmatrix} {}^u\delta\theta_k \\ \tilde{\mathbf{b}}_\omega \\ \Delta\tilde{v} \\ \tilde{\mathbf{b}}_a \\ \Delta\tilde{p} \\ {}^\tau\delta\theta_k \\ \Delta\theta_k \end{bmatrix} + \begin{bmatrix} -\mathbf{I} & \mathbf{0} & \mathbf{0} & \mathbf{0} \\ \mathbf{0} & \mathbf{I} & \mathbf{0} & \mathbf{0} \\ \mathbf{0} & \mathbf{0} & -{}^k_u\check{\mathbf{R}} & \mathbf{0} \\ \mathbf{0} & \mathbf{0} & \mathbf{0} & \mathbf{I} \\ \mathbf{0} & \mathbf{0} & \mathbf{0} & \mathbf{0} \\ \mathbf{0} & \mathbf{0} & \mathbf{0} & \mathbf{0} \\ \mathbf{0} & \mathbf{0} & \mathbf{0} & \mathbf{0} \end{bmatrix} \begin{bmatrix} \mathbf{n}_\omega \\ \mathbf{n}_{\omega b} \\ \mathbf{n}_a \\ \mathbf{n}_{ab} \end{bmatrix}$$

$$\Rightarrow \dot{\mathbf{r}} = \mathbf{F}\mathbf{r} + \mathbf{G}\mathbf{n} \quad (84)$$

where

$$\mathbf{F} = \begin{bmatrix} -[\dot{\hat{\omega}}] & -\mathbf{I} & \mathbf{0} & \mathbf{0} & \mathbf{0} & \mathbf{0} & \mathbf{0} \\ \mathbf{0} & \mathbf{0} & \mathbf{0} & \mathbf{0} & \mathbf{0} & \mathbf{0} & \mathbf{0} \\ -{}^k_u\check{\mathbf{R}}[\dot{\hat{\mathbf{a}}}] & \mathbf{0} & \mathbf{0} & -{}^k_u\check{\mathbf{R}} & \mathbf{0} & -{}^k_u\check{\mathbf{R}}[{}^\tau\check{\mathbf{g}}] & -{}^k_u\check{\mathbf{R}}[{}^\tau\check{\mathbf{g}}] \\ \mathbf{0} & \mathbf{0} & \mathbf{0} & \mathbf{0} & \mathbf{0} & \mathbf{0} & \mathbf{0} \\ \mathbf{0} & \mathbf{0} & \mathbf{I} & \mathbf{0} & \mathbf{0} & \mathbf{0} & \mathbf{0} \\ \mathbf{0} & \mathbf{0} & \mathbf{0} & \mathbf{0} & \mathbf{0} & \mathbf{0} & \mathbf{0} \\ \mathbf{0} & \mathbf{0} & \mathbf{0} & \mathbf{0} & \mathbf{0} & \mathbf{0} & \mathbf{0} \end{bmatrix}$$

In analogy to Equations (63), (64), and (67), we can determine the new state-transition matrix $\Phi(t_{\tau+1}, t_\tau)$ and the new discrete noise covariance. With that, we now propagate the measurement covariance as follows:

$$\mathbf{P}_k = \mathbf{0}_{21 \times 21} \quad (85)$$

$$\mathbf{P}_{\tau+1}^- = \Phi(t_{\tau+1}, t_\tau) \mathbf{P}_\tau \Phi(t_{\tau+1}, t_\tau)^\top + \mathbf{Q}_\tau \quad (86)$$

$$\mathbf{P}_{\tau+1} = \mathbf{B} \mathbf{P}_{\tau+1}^- \mathbf{B}^\top \quad (87)$$

where \mathbf{B} is the cloning matrix that allows us to replace the previous static orientation error ${}^\tau\delta\theta_k$ to the new one ${}^{\tau+1}\delta\theta_k$ when moving to the next measurement time interval, and is given by:

$$\mathbf{B} = \begin{bmatrix} \mathbf{I} & \mathbf{0} & \mathbf{0} & \mathbf{0} & \mathbf{0} & \mathbf{0} & \mathbf{0} \\ \mathbf{0} & \mathbf{I} & \mathbf{0} & \mathbf{0} & \mathbf{0} & \mathbf{0} & \mathbf{0} \\ \mathbf{0} & \mathbf{0} & \mathbf{I} & \mathbf{0} & \mathbf{0} & \mathbf{0} & \mathbf{0} \\ \mathbf{0} & \mathbf{0} & \mathbf{0} & \mathbf{I} & \mathbf{0} & \mathbf{0} & \mathbf{0} \\ \mathbf{0} & \mathbf{0} & \mathbf{0} & \mathbf{0} & \mathbf{I} & \mathbf{0} & \mathbf{0} \\ \mathbf{I} & \mathbf{0} & \mathbf{0} & \mathbf{0} & \mathbf{0} & \mathbf{0} & \mathbf{0} \\ \mathbf{0} & \mathbf{0} & \mathbf{0} & \mathbf{0} & \mathbf{0} & \mathbf{0} & \mathbf{I} \end{bmatrix} \quad (88)$$

The resulting preintegrated measurement covariance is extracted from the top left 15×15 block of \mathbf{P}_{k+1} after the propagation with Equations (85)-(87) over the entire preintegration interval $[t_k, t_{k+1}]$.

3) Preintegration measurement residuals and Jacobians:

We should point out again that this new preintegration depends on the initial orientation ${}^\tau\check{\mathbf{R}}$ for each IMU sampling interval $[t_\tau, t_{\tau+1}]$ (see Equation (77)); and thus, when integrating over one interval to the other, this initial orientation error

changes from ${}^\tau\delta\theta_k$ to ${}^{\tau+1}\delta\theta_k$. This requires extra care when computing the total Jacobian (state transition) matrix, Ψ_{k+1} , over the entire preintegration interval $[t_k, t_{k+1}]$; that is, we propagate this matrix as follows:

$$\Psi_k = \mathbf{I}_{21 \times 21} \quad (89)$$

$$\Psi_{\tau+1} = \mathbf{B} \Phi(t_{\tau+1}, t_\tau) \Psi_\tau \quad (90)$$

Clearly, the total Jacobian matrix Ψ_{k+1} will be the Jacobian of the resulting preintegrated measurement error with respect to the initial error. Therefore, we can simply extract the corresponding blocks to obtain the bias and initial orientation Jacobians. Denoting $\Psi_{k+1}(i, j)$ the 3×3 block of the Jacobian matrix starting at index (i, j) , we have:

$$\mathbf{J}_q = -\Psi_{k+1}(0, 3) \quad (91)$$

$$\mathbf{J}_\alpha = \Psi_{k+1}(12, 3) \quad (92)$$

$$\mathbf{J}_\beta = \Psi_{k+1}(6, 3) \quad (93)$$

$$\mathbf{H}_\alpha = \Psi_{k+1}(12, 9) \quad (94)$$

$$\mathbf{H}_\beta = \Psi_{k+1}(6, 9) \quad (95)$$

$$\mathbf{O}_\alpha = \Psi_{k+1}(12, 18) \quad (96)$$

$$\mathbf{O}_\beta = \Psi_{k+1}(6, 18) \quad (97)$$

where we flip the sign of \mathbf{J}_q to match the same definition used in Model 1 (see Section IV-B3). At this point, using these Jacobians, we can write the new residual associated with the new preintegrated IMU measurement as follows:

$$\mathbf{e}_{IMU}(\mathbf{x}) = \quad (98)$$

$$\begin{bmatrix} 2\text{vec}({}^{k+1}_G\bar{q} \otimes {}^k_G\bar{q}^{-1} \otimes {}^{k+1}_k\check{q}^{-1} \otimes \bar{q}_b) \\ \mathbf{b}_{\omega_{k+1}} - \mathbf{b}_{\omega_k} \\ \left({}^k_G\mathbf{R}({}^G\mathbf{v}_{k+1} - {}^G\mathbf{v}_k) - \mathbf{J}_\beta(\mathbf{b}_{\omega_k} - \mathbf{b}_{\omega_k}^*) - \mathbf{H}_\beta(\mathbf{b}_{a_k} - \mathbf{b}_{a_k}^*) - \mathbf{O}_\beta 2\text{vec}({}^k_G\bar{q} \otimes {}^k_G\bar{q}^{*-1}) - \Delta\check{v} \right) \\ \mathbf{b}_{a_{k+1}} - \mathbf{b}_{a_k} \\ \left({}^k_G\mathbf{R}({}^G\mathbf{p}_{k+1} - {}^G\mathbf{p}_k - {}^G\mathbf{v}_k\Delta T) - \mathbf{J}_\alpha(\mathbf{b}_{\omega_k} - \mathbf{b}_{\omega_k}^*) - \mathbf{H}_\alpha(\mathbf{b}_{a_k} - \mathbf{b}_{a_k}^*) - \mathbf{O}_\alpha 2\text{vec}({}^k_G\bar{q} \otimes {}^k_G\bar{q}^{*-1}) - \Delta\check{p} \right) \end{bmatrix}$$

The resulting measurement Jacobians can be found in Appendix A.2.

V. VISUAL-INERTIAL NAVIGATION

To demonstrate the usability of the proposed continuous preintegration theory presented in the preceding section, In this section, we develop two visual-inertial sensor fusion schemes for visual-inertial navigation systems (VINS) that utilize our inertial preintegration.

A. Tightly-Coupled Indirect VIO

As an IMU-camera sensor suite moves through an unknown environment, visual feature keypoints can be extracted and

tracked from the images to provide motion information about the platform. In particular, the measurement function that maps the 3D position, ${}^G\mathbf{p}_f$, of a feature into the normalized uv-coordinates on the j th-camera's image plane at time step k takes the following form:

$$\mathbf{z}_{fjk} = \Pi \left({}^{C_j}\mathbf{R}_I^k \mathbf{R}_G^k ({}^G\mathbf{p}_f - {}^G\mathbf{p}_k) + {}^{C_j}\mathbf{p}_I \right) + \mathbf{n}_f \quad (99)$$

where ${}^{C_j}\mathbf{R}_I$ and ${}^{C_j}\mathbf{p}_I$ are the rigid IMU-to-camera extrinsic calibration parameters, $\mathbf{n}_f \sim \mathcal{N}(\mathbf{0}, \Lambda_{fjk}^{-1})$, and $\Pi(\cdot)$ is the perspective projection function given by:

$$\Pi \left(\begin{bmatrix} x \\ y \\ z \end{bmatrix} \right) = \begin{bmatrix} x/z \\ y/z \end{bmatrix} \quad (100)$$

The error (or residual) associated with this visual measurement is given by:

$$\mathbf{e}_{fjk}(\mathbf{x}) = \Pi \left({}^{C_j}\mathbf{R}_I^k \mathbf{R}_G^k ({}^G\mathbf{p}_f - {}^G\mathbf{p}_k) + {}^{C_j}\mathbf{p}_I \right) - \mathbf{z}_{fjk} \quad (101)$$

Using these visual measurements along with the preintegrated IMU measurements and marginalization prior, we solve the following optimization problem that tightly couples all available measurement residuals:

$$\hat{\mathbf{x}} = \underset{\mathbf{x}}{\operatorname{argmin}} \left(\|\mathbf{e}_{\text{marg}}(\mathbf{x})\|_2^2 + \sum_{p \in \mathcal{P}} \|\mathbf{e}_{\text{IMU}}(\mathbf{x})\|_{\mathbf{p}_p^{-1}}^2 + \sum_{(f,j,k) \in \mathcal{C}} \|\mathbf{e}_{fjk}(\mathbf{x})\|_{\Lambda_{fjk}}^2 \right) \quad (102)$$

where \mathcal{C} and \mathcal{P} are the set of feature and preintegrated measurements, respectively, while $\mathbf{e}_{\text{marg}}(\mathbf{x})$ is the residual of the marginal prior (see Equation (31)).

1) *Inverse-depth representation*:: A well-known disadvantage of the above representation for features is that points at infinity are difficult to utilize. To mitigate this issue, we instead employ an *inverse-depth* representation (Civera, Davison, and Montiel, 2008). In particular, we represent a feature using the inverse coordinates in the camera frame where it was first observed. Denoting $C_{a,i}$ the frame of reference of the ‘‘anchoring’’ camera, which is associated with the i th camera frame and the anchoring time a , we have the following inverse-depth representation (see Mourikis and Roumeliotis (2007)):

$${}^{C_{a,i}}\mathbf{m}_f = \begin{bmatrix} \alpha \\ \beta \\ \rho \end{bmatrix} \Rightarrow {}^{C_{a,i}}\mathbf{p}_f = \frac{1}{\rho} \begin{bmatrix} \alpha \\ \beta \\ 1 \end{bmatrix} \quad (103)$$

where we also show the relationship between the inverse-depth representation of the feature ${}^{C_{a,i}}\mathbf{m}_f$ and the corresponding 3D position in the anchor frame ${}^{C_{a,i}}\mathbf{p}_f$. The feature position in the j th camera frame at time step k can be computed as follows:

$${}^{C_{k,j}}\mathbf{p}_f = {}^{C_{k,j}}\mathbf{R}_{C_{a,i}} \frac{1}{\rho} \begin{bmatrix} \alpha \\ \beta \\ 1 \end{bmatrix} + {}^{C_{k,j}}\mathbf{p}_{C_{a,i}} \quad (104)$$

$$\begin{aligned} {}^{C_{k,j}}\mathbf{R}_{C_{a,i}} &= {}_I^{C_j}\mathbf{R}^k {}_G^k \mathbf{R}_G^a \mathbf{R}_I^{C_i} \mathbf{R}^\top \\ {}^{C_{k,j}}\mathbf{p}_{C_{a,i}} &= {}_I^{C_j}\mathbf{R}_G^k ({}^G\mathbf{p}_a + {}_G^a \mathbf{R}^\top {}_I \mathbf{p}_{C_i} - {}^G\mathbf{p}_k) + {}^{C_j}\mathbf{p}_I \end{aligned}$$

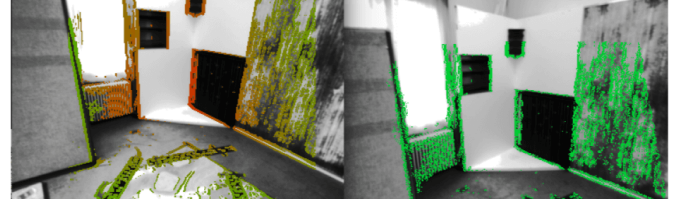


Fig. 4: Visualization of selected depth map pixels with a large intensity gradient (left). Keyframe pixels are projected onto the query frame as a result of the optimized direct alignment of the frame-to-frame relative transformation (right).

Note that due to the nature of the perspective projection (100), $\Pi(\mathbf{x}) = \Pi(\rho\mathbf{x})$, we can multiply both sides of Equation (104) by ρ and have the equivalent measurement model:

$$\mathbf{z}_{fjk} = \Pi(\mathbf{h}) + \mathbf{n}_f \quad (105)$$

$$\mathbf{h} = \begin{bmatrix} h_1 \\ h_2 \\ h_3 \end{bmatrix} := \rho {}^{C_{k,j}}\mathbf{p}_f = \frac{{}^{C_{k,j}}\mathbf{R}_{C_{a,i}}}{\rho} \begin{bmatrix} \alpha \\ \beta \\ 1 \end{bmatrix} + \rho {}^{C_{k,j}}\mathbf{p}_{C_{a,i}} \quad (106)$$

The measurement Jacobians of this inverse-depth model can be found in Appendix B. Note that this measurement model is numerically stable and can handle points at infinity, thus allowing for the gain of the feature direction information from these far-off points.

B. Loosely-Coupled Direct VINS

To further validate the proposed continuous preintegration theory, in the following, by leveraging our prior work (Eckenhoff, Geneva, and Huang, 2017), we develop a *loosely-coupled* VINS algorithm based on direct image alignment and continuous IMU preintegration. In particular, we estimate the relative frame-to-frame motion through direct alignment of image pixels. These relative-motion constraints then allow us to efficiently perform loop closure without explicitly detecting/tracking (or matching) features.

Consider the case where we wish to directly align a current frame C_2 against a keyframe C_1 (see Figure 4). Finding the optimal transformation can be formulated as an optimization problem over the total (warped) pixel intensity difference (i.e., photometric error):

$${}^{C_2}\mathbf{T}_{C_1} = \underset{{}^{C_2}\mathbf{T}_{C_1}}{\operatorname{argmin}} \sum_f \gamma \left(\frac{1}{\sigma_f^2} \left(\underbrace{I_{C_2} \left({}^{C_2}\mathbf{T}_{C_1} {}^{C_1}\mathbf{p}_f \right) - I_{C_1} \left({}^{C_1}\mathbf{p}_f \right)}_{e_f} \right)^2 \right)_{v_f} \quad (107)$$

where ${}^{C_2}\mathbf{T}_{C_1}$ is the transformation between the two camera frames parameterized by the relative quaternion ${}^{C_2}\tilde{q}$ and relative position ${}^{C_1}\mathbf{p}_{C_2}$, while $I_{C_i}(\cdot)$ returns the intensity of a given point projected into the image frame, and $\gamma(\cdot)$ is the Huber cost. The pixel's position in the keyframe, ${}^{C_1}\mathbf{p}_f$ can be found via an online or stereo pair depth map computation. This position is treated as a noisy parameter in the residual

allowing for computation of the residual sigma, σ_r , with the summation being over all pixels f with valid depth estimates and high gradients along the epipolar line. The Huber cost function $\gamma(\cdot)$ with parameter k is defined as (Eade, 2013):

$$\gamma(v) = \begin{cases} v, & \text{if } v < k^2 \\ 2k\sqrt{v} - k^2, & \text{otherwise} \end{cases} \quad (108)$$

The purpose of the Huber cost is to down-weight large residuals which occur naturally in image alignment due to occlusions, and has been used extensively in the literature (e.g., Engel, Schöps, and Cremers (2014)).

Note that the covariance of each residual σ_r^2 encodes the uncertainty due to errors in the intensity measurements as well as the disparity map:

$$\sigma_r^2 = 2\sigma_{int}^2 + \left(\frac{\partial e_f}{\partial d}\right)^2 \sigma_d^2 \quad (109)$$

where σ_{int}^2 denotes the covariance of the intensity reading, $\frac{\partial e_f}{\partial d}$ is the Jacobian of the residual e_f (Equation (107)) with respect to the measured disparity d , and σ_d^2 is the covariance of the disparity measurement. In the case of a depth map computed from a stereo pair as considered in this work, we define \mathbf{t} as the pixel coordinates, z as the pixel depth, and b as the baseline between the stereo pair. The Jacobian $\frac{\partial e_f}{\partial d}$ can be calculated using the chain rule of differentiation as follows (see Equation (107)):

$$\begin{aligned} \frac{\partial e_f}{\partial d} &= \frac{\partial I_{C_2}}{\partial \mathbf{t}} \frac{\partial \mathbf{t}}{\partial C_2 \mathbf{p}_f} \frac{\partial C_2 \mathbf{p}_f}{\partial C_1 \mathbf{p}_f} \frac{\partial C_1 \mathbf{p}_f}{\partial z} \frac{\partial z}{\partial d} \\ &= [I_{C_{2x}} \quad I_{C_{2y}}] \begin{bmatrix} \frac{f_x}{C_2 \mathbf{p}_f(3)} & 0 & -\frac{f_x C_2 \mathbf{p}_f(1)}{C_2 \mathbf{p}_f(3)^2} \\ 0 & \frac{f_y}{C_2 \mathbf{p}_f(3)} & -\frac{f_y C_2 \mathbf{p}_f(2)}{C_2 \mathbf{p}_f(3)^2} \end{bmatrix} \\ &\quad \times \frac{C_1 \mathbf{p}_f}{C_1 \mathbf{R}} \frac{-f_x b}{z} \frac{1}{d^2} \end{aligned} \quad (110)$$

where $I_{C_{2x}}$ and $I_{C_{2y}}$ are the image gradients in the x and y directions respectively, while f_x and f_y are the focal lengths of the camera.

The covariance of the pixel disparity, σ_d^2 , is obtained based on the observation that this disparity is the maximum likelihood estimate for a single measurement graph, with the residual being the difference in intensity between the pixel in the left, I_{C_1L} , and right, I_{C_1R} , images in the keyframe stereo pair, which can be formulated as follows:

$$\check{d} = \underset{d}{\operatorname{argmin}} \frac{1}{\sigma_{rd}^2} \left(I_{C_1L}(v, u) - I_{C_1R}(v, u - d) \right)^2 \quad (111)$$

where the covariance associated with this residual can be found as $\sigma_{rd}^2 = 2\sigma_{int}^2$, and comes from uncertainty in the intensity readings. The covariance on our disparity estimate can then be approximated as:

$$\sigma_d^2 = \left(\frac{\partial e_d}{\partial d} \frac{1}{\sigma_{rd}^2} \right)^{-1} = \sigma_{rd}^2 \left(\frac{1}{I_{C_1R_x}} \right)^2 \quad (112)$$

where $I_{C_1R_x}$ is the x -gradient of the pixel in the right image which is selected as the match.

We solve the direct alignment problem (107) using the Levenberg-Marquadt method. In particular, at each iteration we solve the following normal equation:

$$\begin{aligned} &\left(\left(\sum w_f \mathbf{J}_f^\top \mathbf{J}_f \right) + \lambda \operatorname{diag} \left(\sum w_f \mathbf{J}_f^\top \mathbf{J}_f \right) \right) \delta \frac{C_2}{C_1} \mathbf{T} \\ &= - \sum w_f \mathbf{J}_f^\top e_f \left(\frac{C_2}{C_1} \check{\mathbf{T}} \right) \end{aligned} \quad (113)$$

where λ is the dampening parameter, and $e_f(\frac{C_2}{C_1} \check{\mathbf{T}})$ is the residual due to the f th pixel in the alignment, evaluated at the current estimate (linearization point) for the relative transformation, $\frac{C_2}{C_1} \check{\mathbf{T}}$. The weight w_f is computed at each iteration as follows:

$$w_f = \frac{\partial \gamma(v_f)}{\partial v_f} \frac{1}{\sigma_f^2} \quad (114)$$

$$\frac{\partial \gamma(v_f)}{\partial v_f} = \begin{cases} 1, & \text{if } v_f < k^2 \\ \frac{k}{\sqrt{v_f}}, & \text{otherwise} \end{cases} \quad (115)$$

where v_f is the raw cost fed into the Huber norm (see Equation (107)), and k is a design parameter. The Jacobian matrix \mathbf{J}_f is of the direct alignment measurement residual with respect to the state, computed as:

$$\begin{aligned} \mathbf{J}_f &= [I_{C_{2x}} \quad I_{C_{2y}}] \begin{bmatrix} \frac{f_x}{C_2 \mathbf{p}_f(3)} & 0 & -\frac{f_x C_2 \mathbf{p}_f(1)}{C_2 \mathbf{p}_f(3)^2} \\ 0 & \frac{f_y}{C_2 \mathbf{p}_f(3)} & -\frac{f_y C_2 \mathbf{p}_f(2)}{C_2 \mathbf{p}_f(3)^2} \end{bmatrix} \\ &\quad \times [[C_2 \mathbf{p}_f] \quad -C_1 \mathbf{R}] \end{aligned} \quad (116)$$

After optimization, we will be left with a Gaussian distribution on our estimated relative *camera* pose. We can then transform this into a distribution on the relative *IMU* pose (denoted k and j for the keyframe and query frame IMU states respectively) using covariance propagation:

$$\begin{aligned} \frac{C_2}{C_1} \mathbf{T} &= \frac{C_2}{C_1} \check{\mathbf{T}} \boxplus \frac{C_2}{C_1} \delta \mathbf{T} \\ \text{where } \frac{C_2}{C_1} \delta \mathbf{T} &\sim \mathcal{N}(\mathbf{0}, \Sigma_c) \end{aligned} \quad (117)$$

$$\begin{aligned} \frac{j}{k} \mathbf{T} &= \frac{j}{k} \check{\mathbf{T}} \boxplus \frac{j}{k} \delta \mathbf{T} \\ \text{where } \frac{j}{k} \delta \mathbf{T} &\sim \mathcal{N}(\mathbf{0}, \Sigma_i) \end{aligned} \quad (118)$$

$$\Sigma_i = \frac{\partial \frac{C_2}{C_1} \delta \mathbf{T}}{\partial \frac{j}{k} \delta \mathbf{T}} \Sigma_c \frac{\partial \frac{C_2}{C_1} \delta \mathbf{T}}{\partial \frac{j}{k} \delta \mathbf{T}}^\top \quad (119)$$

where $\Sigma_c = (\sum w_f \mathbf{J}_f^\top \mathbf{J}_f)^{-1}$ is the covariance of the zero-mean alignment error. From this, the relative pose measurement that connects the IMU keyframe and query frame has the following residual:

$$\mathbf{e}_d(\mathbf{x}) = \begin{bmatrix} 2\operatorname{vec} \left(\frac{j}{G} \bar{q} \otimes \frac{k}{G} \bar{q}^{-1} \otimes \frac{j}{k} \check{\bar{q}}^{-1} \right) \\ \frac{k}{G} \mathbf{R} ({}^G \mathbf{p}_j - {}^G \mathbf{p}_k) - \frac{k}{k} \check{\mathbf{p}}_j \end{bmatrix} \quad (120)$$

whose Jacobians with respect to the state are provided in Appendix C, which will be used during graph optimization.

Using this visual measurement residual, along with the preintegrated IMU measurements, we have the following optimization problem for the loosely-coupled direct VINS, which can be solved analogously as in Equation (102):

$$\hat{\mathbf{x}} = \underset{\mathbf{x}}{\operatorname{argmin}} \sum_{d \in \mathcal{D}} \|\mathbf{e}_d(\mathbf{x})\|_{\Sigma_i^{-1}}^2 + \sum_{p \in \mathcal{P}} \|\mathbf{e}_{IMU}(\mathbf{x})\|_{\mathbf{P}_p^{-1}}^2 \quad (121)$$

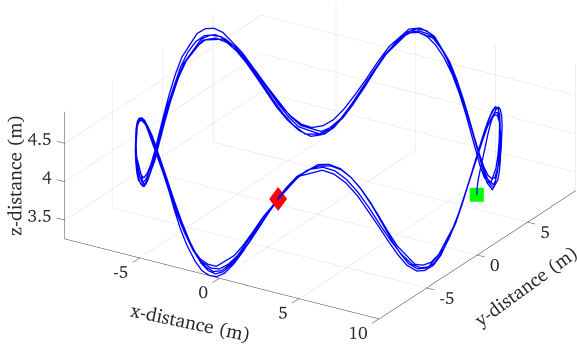


Fig. 5: The ground truth trajectory of a MAV flying in a circle sinusoidal path generated in the Gazebo simulator. The total trajectory length is 307 meters with an average velocity of 6.13 m/s. Start and end positions are denoted with a green square and red diamond, respectively.

where \mathcal{D} and \mathcal{P} are the set of direct alignment relative pose and preintegrated measurements, respectively. Note that this direct image alignment allows for computationally efficient incorporation of large-scale loop closures due to the direct compression of intensity residuals into a single informative relative motion measurement. The ability to perform loop closing is a key advantage over our tightly-coupled VIO system presented in Section V-A as the odometry drifts can be greatly reduced.

VI. MONTE-CARLO SIMULATION ANALYSIS

To validate the proposed continuous preintegration theory, we first perform extensive Monte-Carlo simulations in various conditions in terms of sampling rates and motion dynamics. In particular, to better model the motion dynamics of a physical system, we leverage the open-source Gazebo simulator of a micro air vehicle (MAV) (Koenig and Howard, 2004) which allows for direct realistic simulation and collection of true inertial and pose data (constrained by the physical MAV motion). The simulated datasets were generated as follows: (i) the MAV was commanded to follow a series of waypoints after takeoff, (ii) the ground truth of 100 Hz inertial and pose information was recorded, (iii) 80 synthetic stereo visual feature measurements (uv-coordinates) were created for each camera frame using the true pose information at a static 10Hz frequency. Following the commonly-used IMU model (Trawny and Roumeliotis, 2005), the true inertial measurements were corrupted with an additive discrete bias and white noise using the noise parameters from the VI-Sensor (Nikolic, Rehder, Burri, Gohl, Leutenegger, Furgale, and Siegwart, 2014), while the features' uv-coordinates were corrupted with an additive white noise to each axis with one pixel standard deviation.

In our tests, we used the popular GTSAM (Dellaert, 2012) framework to construct, optimize, and marginalize our graph using the included fixed-lag smoother. To ensure a fair comparison, we evaluate our preintegration methods against the state-of-art discrete preintegration (Forster, Carlone, Dellaert,

and Scaramuzza, 2015, 2017), by using the on-manifold preintegrator class within the GTSAM implementation to compute the required measurement means, bias Jacobians, and covariances. We constructed all graphs side by side, ensuring that the measurements inserted are exactly the same, and thus fair to all methods. For simplicity we used the tightly-coupled indirect features in the graph, in which features are automatically marginalized out after three seconds (that is, no map was created for loop closures, and thus, the system is a VIO system). Note also that we initialized all systems to the ground-truth pose, and with zero bias. Figure 5 shows one example of the true simulated trajectory generated using Gazebo in our simulations.

The Monte-Carlo simulation comparison results of root mean squared error (RMSE) averaged over 50 runs are shown in Figure 6. Evidently, the proposed continuous preintegration using piecewise constant local acceleration model (i.e., Model 2) is slightly better with the RMSE (averaged over all time steps and all runs) of 0.093 meters and 0.300 degrees than that using the piecewise constant measurement model (i.e., Model 1) with the RMSE of 0.096 meters and 0.327 degrees. More importantly, both methods are shown to outperform the discrete state-of-the-art method (Forster, Carlone, Dellaert, and Scaramuzza, 2015, 2017), which has the RMSE of 0.107 meters and 0.328 degrees. It is important to point out that the superior performance (though by small margin in this MAV test, and larger improvement margins expected with higher dynamics not constrained by MAV motion) endowed by the proposed continuous preintegration using the new inertial models over the discrete one does not incur extra computational overhead during graph-based VINS optimization.

Furthermore, we investigate the effect that the IMU frequency has on the relative performance of the preintegration methods under consideration. Using the same simulation setup, the MAV was commanded to follow the trajectory with different Gazebo simulation frequencies. It is important to note that since we are using a physical simulation, the true trajectory will vary from frequency to frequency since the controller will perform differently, however, this is acceptable since we are looking at the relative performance within a given frequency. Table I shows the averaged RMSE results of different IMU frequencies. It can be seen that the proposed continuous preintegration methods have greater impact when the frequency of the IMU is lower (i.e., significantly better performance); while at higher frequencies, the above methods become less distinguishable. This implies that the proposed continuous preintegration methods are better suited for applications with limited IMU frequency, which is often the case for low-cost MEMS sensors.

VII. REAL-WORLD EXPERIMENTAL VALIDATIONS

A. Tightly-Coupled Indirect VIO

In our tightly-coupled VIO system, we use stereo vision due to its superior estimation performance as compared to monocular systems (Paul, Wu, Hesch, Nerurkar, and Roumeliotis, 2017). Stereo correspondences allow for accurate triangulation of features regardless of vehicle motion, making them robust

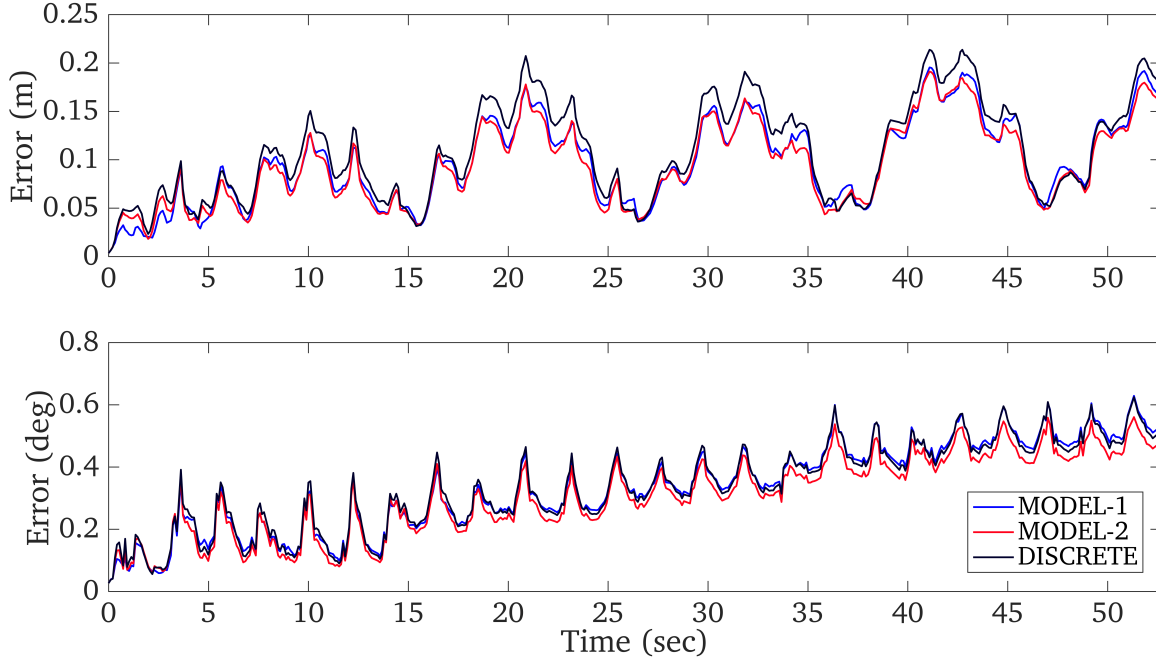


Fig. 6: Monte-Carlo simulation results averaged over 50 runs: (top) position RMSE, and (bottom) orientation RMSE. In this test, physically-realistic synthetic data was generated using a Gazebo MAV simulator. It is clear that the proposed continuous preintegration outperforms the state-of-the-art discrete approach (Forster, Carlone, Dellaert, and Scaramuzza, 2015, 2017).

TABLE I: Analysis of the effect of different IMU frequencies on estimation accuracy. Note that each frequency run has a slightly different trajectory, and thus only the relative spread within a given frequency should be considered.

| | MODEL-1 | | MODEL-2 | | DISCRETE | |
|--------|--------------|-------|--------------|--------------|----------|-------|
| Units | m | deg | m | deg | m | deg |
| 100 Hz | 0.096 | 0.327 | 0.093 | 0.300 | 0.107 | 0.328 |
| 200 Hz | 0.051 | 0.204 | 0.049 | 0.179 | 0.058 | 0.207 |
| 400 Hz | 0.033 | 0.107 | 0.033 | 0.101 | 0.035 | 0.109 |
| 800 Hz | 0.030 | 0.085 | 0.030 | 0.085 | 0.031 | 0.086 |

to maneuvers troubling monocular systems such as hovering. In addition, stereo allows for a direct reading of the scale, which is highly informative to the estimator.

When a pair of stereo images arrives, we perform feature extraction and description using the OpenCV implementation of ORB features, which offers both superior speed against other descriptor methods as well as robust performance (Bradski, 2000; Rublee, Rabaud, Konolige, and Bradski, 2011). In order to uniformly find features across each image, we divide them into 9 regions and perform descriptor extraction in parallel. From these descriptors, we use the OpenCV function `BFMatcher` for brute force descriptor matching. This matching is performed between the currently active features' descriptors to both the left and right image, yielding both left-to-left and right-to-right tracks. We also perform matching between the currently extracted descriptors in the left and right images in order to find stereo correspondences. For the temporal correspondence sets, we use eight-point RANSAC for outlier rejection, while for the new stereo left-to-right matches, outliers are rejected based on the stereo epipolar

constraint.

If an active feature is successfully tracked, the normalized image coordinates are added as measurements associated with that feature. We maintain 500 active features at any time. If the number of successfully tracked features falls below this threshold, we initialize new ones using left-to-right matches of descriptors that have not already been associated to a feature. If, after this process, we still have under 500 features, we then initialize monocular features from descriptors in the new left and right images that have neither been associated with a previous feature or have been involved in a stereo match. If a stereo correspondence that relates two monocular features is found, we merge them into a single stereo feature.

Inspired by Leutenegger, Lynen, Bosse, Siegwart, and Furgale (2015), we maintain two sliding windows of IMU states in the estimator. The first, denoted as the inertial window, contains the full 15 DOF IMU state and refers to the most recent imaging times. The second window, called the pose window, contains a set of pose-only clones (that is, only the orientation and position are maintained). At every imaging time we create a new corresponding IMU node. The IMU readings collected over the interval are preintegrated to both predict the new state and to form a preintegrated IMU measurement between the previous and new state.

After tracking, we formulate the batch optimization (i.e., BA) problem using all features with a sufficient number of tracks as well as all nodes in the inertial and pose windows. The measurements contained in this graph are: (i) the prior, (ii) the image coordinate measurements for the active features, and (iii) the preintegration factors between the inertial window states (see Equation (102)). We use the Ceres Solver with an

TABLE II: Average absolute RMSE results of the tightly-coupled indirect VINS for the EurocMav datasets averaged over 10 runs. All systems were initialized with the ground truth state.

| Units | MODEL-1 | | MODEL-2 | | OKVIS | |
|------------|--------------|--------------|--------------|--------------|--------------|--------------|
| | m | deg | m | deg | m | deg |
| V1_01_easy | 0.192 | 2.796 | 0.190 | 2.718 | 0.217 | 2.445 |
| V1_02_med | 0.175 | 0.862 | 0.188 | 1.012 | 0.192 | 1.728 |
| V1_03_diff | 0.189 | 3.801 | 0.190 | 2.500 | 0.159 | 3.475 |
| V2_01_easy | 0.130 | 1.193 | 0.119 | 1.240 | 0.160 | 0.851 |
| V2_02_med | 0.206 | 2.123 | 0.223 | 2.431 | 0.139 | 1.612 |
| V2_03_diff | 0.524 | 3.495 | 0.525 | 2.929 | 0.270 | 6.725 |

elimination ordering that takes advantage of the sparsity of the problem through the Schur Complement (Agarwal, Mierle, and Others, 2018; Kummerle, Grisetti, Strasdat, Konolige, and Burgard, 2011).

If the inertial window has reached its max length, we flag the oldest state’s velocity and biases for marginalization. If the pose window also reaches its max length, we add both the oldest pose and all features it has seen into the marginal state list. Performing marginalization yields a new prior factor that has absorbed the old prior, the marginalized feature measurements, and the oldest preintegration factor. The oldest IMU state whose velocity and biases have been marginalized is then moved into the pose window.

1) *EurocMav datasets*:: We compared our tightly-coupled indirect VIO system with a state-of-the-art open-source VINS – that is, the Open Keyframe-based Visual-Inertial SLAM (OKVIS) (Leutenegger, Lynen, Bosse, Siegwart, and Furgale, 2015), although several different VINS methods were recently introduced (e.g., Bloesch, Burri, Omari, Hutter, and Siegwart (2017)). We performed this comparison on the EurocMav datasets (Burri, Nikolic, Gohl, Schneider, Rehder, Omari, Achtelek, and Siegwart, 2016), which have become the standard method for evaluating VINS algorithms. We ran our preintegration-based system as well as stereo-OKVIS with inertial and pose/keyframe windows of 6 and 15, and 6 and 8, respectively. These parameters were selected to ensure real-time performance with both systems having minimal dropped frames. It should be noted that depending on the tuning parameters used in the VINS algorithms, their performance may vary (e.g., see Delmerico and Scaramuzza (2018)). Note also that our VIO system uses a sliding window of poses as well as the inertial window connected with preintegrated measurements but does *not* keep any kind of map (to allow intra-window loop closures), while OKVIS employs a set of keyframes where mapped points are maintained. Nevertheless, to provide a direct comparison, we initialize both systems with the true orientation, biases, velocity, and position such that no post-processing yaw alignment is needed.

A representative run from the “V1_02_med” dataset can be seen in Figure 7a where we plot the estimated trajectories of our VIO and OKVIS along with the ground truth. Note that it is understood that the performance of VINS algorithms may vary even if re-running on the same dataset due to some randomness in visual tracking (e.g., RANSAC); and

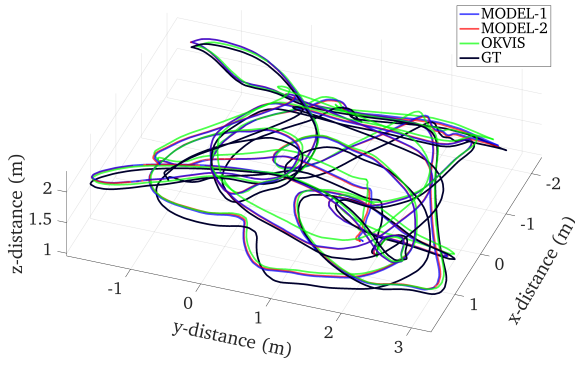
thus, we repeated the test for 10 times and averaged the results in order to better evaluate the relative performance of the compared approaches. Figure 7b shows the RMSE results of our VIO algorithm based on the proposed continuous preintegration with the two models as compared to OKVIS, which were computed at every time step and then averaged over all the runs; while the averaged RMSE results are shown in Table II. These results clearly demonstrate that our VIO system can offer competitive performance to OKVIS; that is, we see instances where our method outperforms OKVIS, while in others OKVIS is superior. Between the two proposed preintegration models, this trend is similar, as they both have trajectories where they outperform the other.

2) *Large-scale indoor datasets*:: We further performed large-scale (as compared to the EurocMav datasets) indoor experiments in two buildings at the University of Delaware (UD) using our hand-held VI-Sensor. In these experiments, because no ground truth was available, we initialized the system by keeping the device stationary for a short period of time (e.g., 2 seconds) so that the initial orientation and biases could be found, while the position and velocities were initialized as zero. The first indoor experiment was performed in the UD Gore Hall, in which the trajectory starts on the first floor, traverses the staircase to the third floor, and returns to the bottom floor, making a loop on each level. To evaluate the estimation performance the trajectory returns to the original starting location. The 3D trajectory estimate is shown in Figure 8a while its projection onto the building floor plan is shown in Figure 8b. For the first preintegration model (Model 1), the estimated trajectory returned to within 0.484 meters of the starting location over a trajectory of 240 meters (0.20% of the path), while the second model (Model 2) had an error of only 0.330 meters (0.14%).

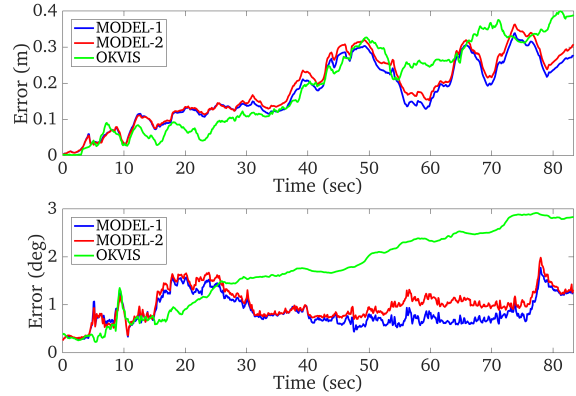
The second indoor experiment was conducted in the UD Smith Hall. Starting on the second floor, we traversed along a rectangular wall before descending the stairs, looping around the first floor, then returning up the stairs, looping one and a half times around the upper level before returning to the starting position. In this test, the final error of the estimated trajectory using the first preintegration model (Model 1) was 1.54 meters across the approximately 240 meter long trajectory (0.64% of the path). Meanwhile, the second preintegration model (Model 2) had an error of 2.625 meters (1.09% of the path). Note that both results are worse than those in the first experiment, primarily due to the fact that during this test, there were people walking around, lighting conditions were varying, and some parts of the environment lacked good features to detect and track (see Figure 9a). The 3D trajectory estimate and its projection onto the floor plan are shown in Figures 9b and 9c, respectively. These results clearly demonstrate that our VIO systems using the proposed continuous preintegration are able to perform accurate 3D motion tracking in relatively large-scale complex environments.

B. Loosely-Coupled Direct VINS

When a stereo pair arrives, as in the preceding indirect VIO, we perform the proposed continuous preintegration from

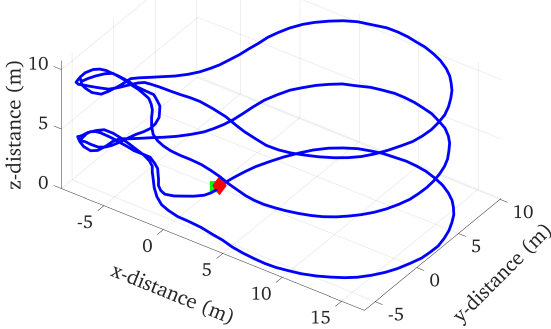
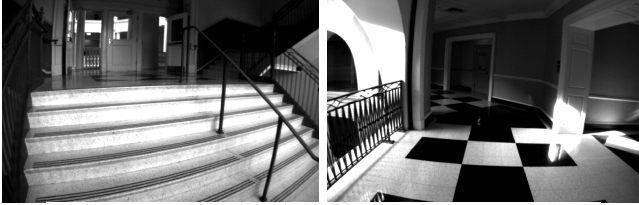


(a) The trajectory estimates.

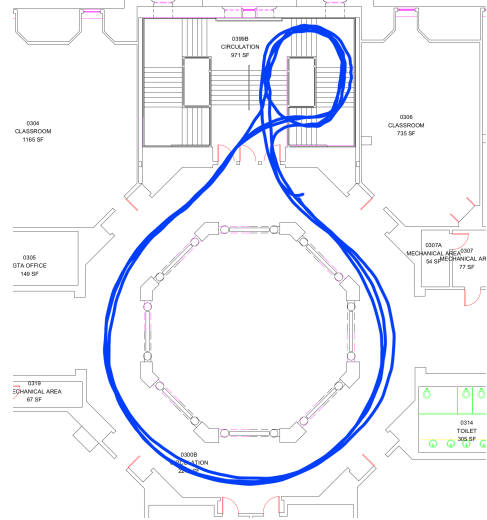


(b) The position and orientation RMSE.

Fig. 7: A typical run and the corresponding RMSE results of the proposed VIO using the two preintegration models and OKVIS for the “V1_02_med” EurocMav dataset which has a total trajectory length of 76 meters.



(a) Example images (top) and 3D trajectory (bottom).



(b) Projection of the estimated trajectory onto the floor plan.

Fig. 8: The trajectory estimates of the indoor experiment performed in the UD Gore Hall. Two example images from the dataset can be seen in (a), while the starting and ending locations are shown by a green square and red diamond in the plot, respectively. Note that the three floors have similar layouts, and thus only one floor plan is shown in plot (b).

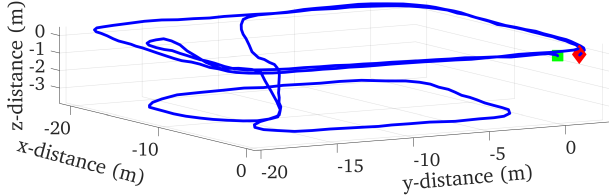
the previous IMU state to the current state. We then check the list of stored keyframes for a suitable candidate for direct image alignment, based on a field-of-view constraint between the candidate and the current image. If no such acceptable candidate is found, a new keyframe is created from the previous image pair and its depth map is computed using the OpenCV function `StereoSGBM`. In particular, in order to perform coarse-to-fine alignment, the depth map is computed for multiple image pyramid levels. Starting at the coarsest image level, we perform iterative image alignment, using the larger levels to further refine the coarse image alignment transform. This image alignment optimization was implemented in a CUDA kernel for GPU acceleration, thus allowing for the system to achieve real-time performance. After convergence, we recover the relative-pose constraint and add it as a factor to our direct-VINS graph. Note that as

compared to our indirect VIO method, we do not perform marginalization and thus allow later incorporation of loop closures. To handle this increase of computational complexity and allow for real-time performance, we leverage the iSAM2 incremental smoothing implementation within the GTSAM framework (Kaess, Johannsson, Roberts, Ila, Leonard, and Dellaert, 2012; Dellaert, 2012). However, the proposed framework is by no means optimal and can be further refined, for example, by more intelligently selecting keyframes.

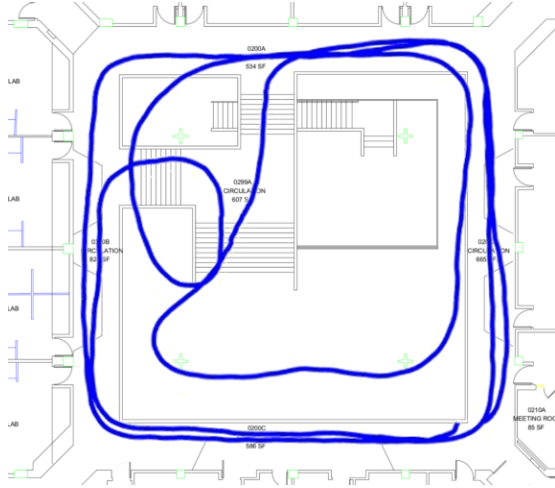
1) EurocMav datasets:: To validate our direct VINS approach, we perform tests on the same EurocMav datasets as before, which allow for direct comparison to a ground-truth trajectory (Burri, Nikolic, Gohl, Schneider, Rehder, Omari, Achtelik, and Siegwart, 2016). The results of the proposed direct VINS using two different preintegration models are shown in Table III. Clearly, in scenarios in which a large



(a) Two sample images seen during the experiment.



(b) View of the estimated 3D trajectory.



(c) Projection of the estimated trajectory onto the floor plan.

Fig. 9: The results of the indoor experiment performed in the UD Smith Hall. Two example left camera images are shown in (a). In plot (b), the starting and ending locations of the trajectory estimates are shown as a green square and red diamond, respectively. Note that the trajectory shown in (c) occurs on both the second and first floors.

TABLE III: Average absolute RMSE results for the Euroc-Mav datasets over 10 runs using the proposed direct VINS algorithm. All systems were initialized with the ground truth state.

| Units | MODEL-1 | | MODEL-2 | |
|------------|--------------|--------------|--------------|--------------|
| | m | deg | m | deg |
| V1_01_easy | 0.245 | 2.263 | 0.239 | 2.280 |
| V1_02_med | 0.154 | 1.898 | 0.143 | 1.652 |
| V1_03_diff | 0.111 | 1.176 | 0.119 | 1.325 |
| V2_01_easy | 0.165 | 1.734 | 0.165 | 2.271 |
| V2_02_med | 0.153 | 2.446 | 0.160 | 2.395 |
| V2_03_diff | 0.906 | 3.396 | 0.946 | 6.037 |

amount of loop closures are present (e.g., “V1_02_med” and “V1_03_diff”), this system can outperform the tightly-coupled VIO system (see Section V-A and Table II). However, when such loop closures are not available, the loosely-coupled systems suffer from larger drifts, as can be seen from the result of “V2_01_easy”.

For these particular datasets, Model 1 appears to be a better choice. This may be due to the fact that Model 2 linearizes about the initial orientation and could be susceptible to large angle updates when loop closure occurs. In addition, the proposed direct VINS is sensitive to the tuning parameters, which in this experiment were chosen as *identical* across all datasets, rather than finding an optimal set per scenario. This led to situations such as “V2_03_diff”, in which some of the runs yield incorrect loop closures despite our system attempting to reject these, greatly corrupting the resulting trajectory estimates. However, as the purpose of this work is to show the accuracy of the proposed preintegration, instead of the robustness of the utilized front-ends, these results along with the previous simulation results strongly suggest that our preintegration models can be, and should be, used when designing graph-based VINS.

VIII. CONCLUSIONS AND FUTURE WORK

In this paper, we have analytically derived continuous inertial preintegration and successfully applied it to graph-based visual-inertial navigation systems (VINS). In particular, we advocate two new preintegration models for the evolution of IMU measurements across sampling intervals. In the first, we assume that the inertial measurements remain piecewise constant; while in the second, we incorporate a piecewise constant *local* acceleration model into the preintegration framework. We have validated through extensive Monte-Carlo simulations that both models outperform the state-of-the-art *discrete* preintegration. Furthermore, we have utilized this continuous preintegration theory and developed two different VINS algorithms primarily to show the advantages of the proposed preintegration. In the first, we formulated an indirect (feature-based), tightly-coupled, sliding-window optimization based VIO system that offers competitive (if not better) performance to a state-of-the-art graph-based VINS algorithm. The second VINS method was developed instead based on loosely-coupled direct image alignment with the proposed preintegrations, allowing for efficient incorporation of informative loop closures.

In the future, we will integrate the proposed continuous preintegrations to aided inertial navigation systems with other aiding sources (e.g., LiDAR). We also seek to further robustify our VINS to handle more challenging scenarios (e.g., ultra-fast motion and highly-dynamic scenes).

ACKNOWLEDGMENTS

This work was partially supported by the University of Delaware College of Engineering, the NSF (IIS-1566129), and the DTRA (HDTRA1-16-1-0039).

REFERENCES

- A. I. Mourikis, N. Trawny, S. I. Roumeliotis, A. E. Johnson, and L. H. Matthies, "Vision-aided inertial navigation for precise planetary landing: Analysis and experiments," in *Robotics: Science and Systems*, 2007.
- L. Ellekilde, "Dense 3D Map Construction for Indoor Search and Rescue," *Journal of Field Robotics*, vol. 24, no. 1-2, p. 71, 2007.
- A. Geiger, P. Lenz, and R. Urtasun, "Are we ready for autonomous driving? the kitti vision benchmark suite," in *Computer Vision and Pattern Recognition (CVPR), 2012 IEEE Conference on*. IEEE, 2012, pp. 3354–3361.
- C. Cadena, L. Carlone, H. Carrillo, Y. Latif, D. Scaramuzza, J. Neira, I. D. Reid, and J. J. Leonard, "Past, present, and future of simultaneous localization and mapping: Toward the robust-perception age," *IEEE Transactions on Robotics*, vol. 32, no. 6, pp. 1309–1332, 2016.
- Y. Ling, T. Liu, and S. Shen, "Aggressive quadrotor flight using dense visual-inertial fusion," in *Robotics and Automation (ICRA), 2016 IEEE International Conference on*. IEEE, 2016, pp. 1499–1506.
- K. J. Wu, A. M. Ahmed, G. A. Georgiou, and S. I. Roumeliotis, "A square root inverse filter for efficient vision-aided inertial navigation on mobile devices," in *2015 Robotics: Science and Systems Conference, RSS 2015*. MIT Press Journals, 2015.
- A. I. Mourikis and S. I. Roumeliotis, "A multi-state constraint Kalman filter for vision-aided inertial navigation," in *Proceedings of the IEEE International Conference on Robotics and Automation*, Rome, Italy, Apr. 10–14, 2007, pp. 3565–3572.
- T. Lupton and S. Sukkarieh, "Visual-inertial-aided navigation for high-dynamic motion in built environments without initial conditions," *IEEE Transactions on Robotics*, vol. 28, no. 1, pp. 61–76, 2012.
- C. Forster, L. Carlone, F. Dellaert, and D. Scaramuzza, "Imu preintegration on manifold for efficient visual-inertial maximum-a-posteriori estimation," in *Robotics: Science and Systems*. Georgia Institute of Technology, 2015.
- , "On-manifold preintegration for real-time visual-inertial odometry," *IEEE Transactions on Robotics*, vol. 33, no. 1, pp. 1–21, 2017.
- K. Eickenhoff, P. Geneva, and G. Huang, "High-accuracy preintegration for visual-inertial navigation," in *Proc. of the International Workshop on the Algorithmic Foundations of Robotics*, San Francisco, CA, Dec. 13–16, 2016.
- N. Trawny and S. I. Roumeliotis, "Indirect Kalman filter for 3D attitude estimation," University of Minnesota, Dept. of Comp. Sci. & Eng., Tech. Rep., Mar. 2005.
- Y. Yang, J. Maley, and G. Huang, "Null-space-based marginalization: Analysis and algorithm," in *Proc. IEEE/RSJ International Conference on Intelligent Robots and Systems*, Vancouver, Canada, Sep. 24–28, 2017.
- S. I. Roumeliotis and J. W. Burdick, "Stochastic cloning: A generalized framework for processing relative state measurements," in *Proceedings of the IEEE International Conference on Robotics and Automation*, Washington, DC, May 11–15 2002, pp. 1788–1795.
- J. Hesch, D. Kottas, S. Bowman, and S. Roumeliotis, "Consistency analysis and improvement of vision-aided inertial navigation," *IEEE Transactions on Robotics*, vol. PP, no. 99, pp. 1–19, 2013.
- C. X. Guo and S. I. Roumeliotis, "Imu-rgbd camera navigation using point and plane features," in *2013 IEEE/RSJ International Conference on Intelligent Robots and Systems (IROS)*. IEEE, 2013, pp. 3164–3171.
- C. X. Guo, D. G. Kottas, R. DuToit, A. Ahmed, R. Li, and S. I. Roumeliotis, "Efficient visual-inertial navigation using a rolling-shutter camera with inaccurate timestamps," in *Robotics: Science and Systems*. Citeseer, 2014.
- R. Kummerle, G. Grisetti, H. Strasdat, K. Konolige, and W. Burgard, "g2o: A general framework for graph optimization," in *Proc. of the IEEE International Conference on Robotics and Automation*, Shanghai, China, May 9–13, 2011, pp. 3607–3613.
- S. Leutenegger, S. Lynen, M. Bosse, R. Siegwart, and P. Furgale, "Keyframe-based visual-inertial odometry using non-linear optimization," *The International Journal of Robotics Research*, vol. 34, no. 3, pp. 314–334, 2015.
- R. Mur-Artal and J. D. Tardós, "Orb-slam2: An open-source slam system for monocular, stereo, and rgb-d cameras," *IEEE Transactions on Robotics*, vol. 33, no. 5, pp. 1255–1262, 2017.
- J. Engel, T. Schöps, and D. Cremers, "Lsd-slam: Large-scale direct monocular slam," in *European Conference on Computer Vision*. Springer, 2014, pp. 834–849.
- J. Engel, J. Stückler, and D. Cremers, "Large-scale direct slam with stereo cameras," in *Intelligent Robots and Systems (IROS), 2015 IEEE/RSJ International Conference on*. IEEE, 2015, pp. 1935–1942.
- D. Caruso, J. Engel, and D. Cremers, "Large-scale direct slam for omnidirectional cameras," in *Intelligent Robots and Systems (IROS), 2015 IEEE/RSJ International Conference on*. IEEE, 2015, pp. 141–148.
- J. Engel, V. Koltun, and D. Cremers, "Direct sparse odometry," *IEEE Transactions on Pattern Analysis and Machine Intelligence*, vol. 40, no. 3, pp. 611–625, 2018.
- R. Wang, M. Schwörer, and D. Cremers, "Stereo dso: Large-scale direct sparse visual odometry with stereo cameras," in *International Conference on Computer Vision (ICCV), Venice, Italy, 2017*.
- M. Bloesch, S. Omari, M. Hutter, and R. Siegwart, "Robust visual inertial odometry using a direct ekf-based approach," in *Intelligent Robots and Systems (IROS), 2015 IEEE/RSJ International Conference on*. IEEE, 2015, pp. 298–304.
- M. Bloesch, M. Burri, S. Omari, M. Hutter, and R. Siegwart, "Iterated extended kalman filter based visual-inertial odometry using direct photometric feedback," *The International Journal of Robotics Research*, vol. 36, no. 10, pp. 1053–1072, 2017.
- V. Usenko, J. Engel, J. Stückler, and D. Cremers, "Direct visual-inertial odometry with stereo cameras," in *Robotics and Automation (ICRA), 2016 IEEE International Conference on*. IEEE, 2016, pp. 1885–1892.
- S. Shen, N. Michael, and V. Kumar, "Tightly-coupled monoc-

ular visual-inertial fusion for autonomous flight of rotorcraft mavs,” in *Robotics and Automation (ICRA), 2015 IEEE International Conference on*. IEEE, 2015, pp. 5303–5310.

T. Qin, P. Li, and S. Shen, “Vins-mono: A robust and versatile monocular visual-inertial state estimator,” *CoRR*, vol. abs/1708.03852, 2017.

K. Eickenhoff, P. Geneva, and G. Huang, “Direct visual-inertial navigation with analytical preintegration,” in *Proc. of the IEEE International Conference on Robotics and Automation*, Singapore, May 29–Jun.3, 2017.

C. Hertzberg, R. Wagner, U. Frese, and L. Schröder, “Integrating generic sensor fusion algorithms with sound state representations through encapsulation of manifolds,” *Information Fusion*, vol. 14, no. 1, pp. 57–77, 2013.

G. Huang, M. Kaess, and J. Leonard, “Consistent sparsification for graph optimization,” in *Proc. of the European Conference on Mobile Robots*, Barcelona, Spain, Sep. 25–27 2013, pp. 150–157.

K. Eickenhoff, L. Paull, and G. Huang, “Decoupled, consistent node removal and edge sparsification for graph-based SLAM,” in *Proc. IEEE/RSJ International Conference on Intelligent Robots and Systems*, Daejeon, Korea, Oct. 9–14, 2016, pp. 3275–3282.

G. Huang, A. I. Mourikis, and S. I. Roumeliotis, “An observability constrained sliding window filter for SLAM,” in *Proc. of the IEEE/RSJ International Conference on Intelligent Robots and Systems*, San Francisco, CA, Sep. 25–30 2011, pp. 65–72.

E. Nerurkar, K. Wu, and S. Roumeliotis, “C-KLAM: Constrained keyframe-based localization and mapping,” in *Robotics and Automation (ICRA), 2014 IEEE International Conference on*, May 2014, pp. 3638–3643.

A. B. Chatfield, *Fundamentals of High Accuracy Inertial Navigation*. Reston, VA: American Institute of Aeronautics and Astronautics, Inc., 1997.

K. Eickenhoff, P. Geneva, and G. Huang, “Continuous preintegration theory for visual-inertial navigation,” University of Delaware, Tech. Rep. RPNG-2018-CPI, 2018, available: http://udel.edu/~ghuang/papers/tr_cpi.pdf.

J. Civera, A. Davison, and J. Montiel, “Inverse depth parametrization for monocular SLAM,” *IEEE Transactions on Robotics*, vol. 24, no. 5, pp. 932–945, Oct. 2008.

E. Eade, “Gauss-newton / levenberg-marquardt optimization,” *Technical Report*, 2013.

N. Koenig and A. Howard, “Design and use paradigms for gazebo, an open-source multi-robot simulator,” in *Intelligent Robots and Systems, 2004. (IROS 2004). Proceedings. 2004 IEEE/RSJ International Conference on*, vol. 3. IEEE, 2004, pp. 2149–2154.

J. Nikolic, J. Rehder, M. Burri, P. Gohl, S. Leutenegger, P. T. Furgale, and R. Siegwart, “A synchronized visual-inertial sensor system with fpga pre-processing for accurate real-time slam,” in *Robotics and Automation (ICRA), 2014 IEEE International Conference on*. IEEE, 2014, pp. 431–437.

F. Dellaert, “Factor graphs and gtsam: A hands-on introduction,” Georgia Institute of Technology, Tech. Rep., 2012.

M. K. Paul, K. Wu, J. A. Hesck, E. D. Nerurkar, and S. I. Roumeliotis, “A comparative analysis of tightly-coupled

monocular, binocular, and stereo vins,” in *Robotics and Automation (ICRA), 2017 IEEE International Conference on*. IEEE, 2017, pp. 165–172.

G. Bradski, “Open source computer vision (OpenCV) library,” *Dr. Dobbs’s Journal of Software Tools*, 2000.

E. Rublee, V. Rabaud, K. Konolige, and G. Bradski, “ORB: An efficient alternative to SIFT or SURF,” in *Proceedings of the 2011 International Conference on Computer Vision*, Washington, DC, 2011, pp. 2564–2571.

S. Agarwal, K. Mierle, and Others, “Ceres solver,” <http://ceres-solver.org>, 2018.

M. Burri, J. Nikolic, P. Gohl, T. Schneider, J. Rehder, S. Omari, M. W. Achtelik, and R. Siegwart, “The euroc micro aerial vehicle datasets,” *The International Journal of Robotics Research*, vol. 35, no. 10, pp. 1157–1163, 2016.

J. Delmerico and D. Scaramuzza, “A benchmark comparison of monocular visual-inertial odometry algorithms for flying robots,” in *Proc. of the IEEE International Conference on Robotics and Automation*, Brisbane, Australia, May 21–25, 2018.

M. Kaess, H. Johannsson, R. Roberts, V. Ila, J. Leonard, and F. Dellaert, “iSAM2: Incremental smoothing and mapping using the Bayes tree,” *International Journal of Robotics Research*, vol. 31, pp. 217–236, Feb. 2012.

APPENDIX A: PREINTEGRATION MEASUREMENT JACOBIANS

A.1. Model 1 Measurement Jacobians

We first partition the preintegrated measurement residual as follows:

$$\mathbf{e}_{IMU}(\mathbf{x}) = [\mathbf{e}_\theta^\top \quad \mathbf{e}_{b_\omega}^\top \quad \mathbf{e}_v^\top \quad \mathbf{e}_{b_a}^\top \quad \mathbf{e}_p^\top]^\top \quad (122)$$

The measurement Jacobian with respect to each element of the error state vector can be found by perturbing the measurement function for the corresponding element. For example, the relative-rotation measurement residual \mathbf{e}_θ is perturbed by a small change in gyro bias around the current estimate, i.e., $\mathbf{b}_{\omega_k} - \mathbf{b}_{\omega_k}^* = \hat{\mathbf{b}}_{\omega_k} + \delta \mathbf{b}_{\omega_k} - \mathbf{b}_{\omega_k}^*$, which yields (see Equation (69)):

$$\begin{aligned} \mathbf{e}_\theta &= 2\text{vec} \left(\begin{matrix} \hat{q}^{k+1} \otimes \hat{q}^{k-1} \otimes \hat{q}^{k+1} \otimes \left[\frac{\mathbf{J}_q(\hat{\mathbf{b}}_{\omega_k} + \delta \mathbf{b}_{\omega_k} - \mathbf{b}_{\omega_k}^*)}{2} \right] \\ 1 \end{matrix} \right) \\ &=: 2\text{vec} \left(\hat{q}_r \otimes \left[\frac{\mathbf{J}_q(\hat{\mathbf{b}}_{\omega_k} + \delta \mathbf{b}_{\omega_k} - \mathbf{b}_{\omega_k}^*)}{2} \right] \right) \\ &= 2\text{vec} \left(\mathcal{L}(\hat{q}_r) \left[\frac{\mathbf{J}_q(\hat{\mathbf{b}}_{\omega_k} + \delta \mathbf{b}_{\omega_k} - \mathbf{b}_{\omega_k}^*)}{2} \right] \right) \\ &= 2\text{vec} \left(\begin{bmatrix} \hat{q}_{r,4} \mathbf{I}_{3 \times 3} - [\hat{\mathbf{q}}_r] & \hat{\mathbf{q}}_r \\ -\hat{\mathbf{q}}_r^\top & \hat{q}_{r,4} \end{bmatrix} \left[\frac{\mathbf{J}_q(\hat{\mathbf{b}}_{\omega_k} + \delta \mathbf{b}_{\omega_k} - \mathbf{b}_{\omega_k}^*)}{2} \right] \right) \\ &= (\hat{q}_{r,4} \mathbf{I}_{3 \times 3} - [\hat{\mathbf{q}}_r]) \mathbf{J}_q(\hat{\mathbf{b}}_{\omega_k} + \delta \mathbf{b}_{\omega_k} - \mathbf{b}_{\omega_k}^*) + \text{other terms} \end{aligned} \quad (123)$$

As a result, the Jacobian with respect to a perturbation in bias can be read out as:

$$\frac{\partial \mathbf{e}_\theta}{\partial \delta \mathbf{b}_{\omega_k}} = (\hat{q}_{r,4} \mathbf{I}_{3 \times 3} - [\hat{\mathbf{q}}_r]) \mathbf{J}_q \quad (124)$$

Proceeding analogously, the Jacobian with respect to $^{k+1}\delta\theta_G$ can be found as follows:

$$\begin{aligned}
\mathbf{e}_\theta &= 2\text{vec} \left(\begin{bmatrix} \frac{k+1}{2}\delta\theta_G \\ 1 \end{bmatrix} \otimes \hat{q}^{k+1} \otimes \hat{q}^{k+1} \otimes \hat{q}^{k+1} \otimes \hat{q}^{k+1} \right) \\
&=: 2\text{vec} \left(\begin{bmatrix} \frac{k+1}{2}\delta\theta_G \\ 1 \end{bmatrix} \otimes \hat{q}_{rb} \right) \\
&= 2\text{vec} \left(\mathcal{R}(\hat{q}_{rb}) \begin{bmatrix} \frac{k+1}{2}\delta\theta_G \\ 1 \end{bmatrix} \right) \\
&= 2\text{vec} \left(\begin{bmatrix} \hat{q}_{rb,4}\mathbf{I}_{3\times 3} + [\hat{\mathbf{q}}_{rb}] & \hat{\mathbf{q}}_{rb} \\ -\hat{\mathbf{q}}_{rb}^\top & \hat{q}_{rb,4} \end{bmatrix} \begin{bmatrix} \frac{1}{2}^{k+1}\delta\theta_G \\ 1 \end{bmatrix} \right) \\
&= (\hat{q}_{rb,4}\mathbf{I}_{3\times 3} + [\hat{\mathbf{q}}_{rb}])^{k+1}\delta\theta_G + \text{other terms} \\
\Rightarrow \frac{\partial \mathbf{e}_\theta}{\partial^{k+1}\delta\theta_G} &= \hat{q}_{rb,4}\mathbf{I}_{3\times 3} + [\hat{\mathbf{q}}_{rb}] \quad (125)
\end{aligned}$$

Similarly, the Jacobian with respect to $^k\delta\theta_G$ is computed by:

$$\begin{aligned}
\mathbf{e}_\theta &= 2\text{vec} \left(\hat{q}^{k+1} \otimes \hat{q}^{k+1} \otimes \begin{bmatrix} -\frac{k}{2}\delta\theta_G \\ 1 \end{bmatrix} \otimes \hat{q}^{k+1} \otimes \hat{q}^{k+1} \right) \\
&=: 2\text{vec} \left(\hat{q}_n \otimes \begin{bmatrix} -\frac{k}{2}\delta\theta_G \\ 1 \end{bmatrix} \otimes \hat{q}_{mb}^{-1} \right) \\
&= 2\text{vec} \left(\mathcal{L}(\hat{q}_n)\mathcal{R}(\hat{q}_{mb}^{-1}) \begin{bmatrix} -\frac{k}{2}\delta\theta_G \\ 1 \end{bmatrix} \right) \\
&= 2\text{vec} \left(\begin{bmatrix} \hat{q}_{n,4}\mathbf{I}_{3\times 3} - [\hat{\mathbf{q}}_n] & \hat{\mathbf{q}}_n \\ -\hat{\mathbf{q}}_n^\top & \hat{q}_{n,4} \end{bmatrix} \times \right. \\
&\quad \left. \begin{bmatrix} \bar{q}_{mb,4}\mathbf{I}_{3\times 3} - [\bar{\mathbf{q}}_{mb}] & -\bar{\mathbf{q}}_{mb} \\ \bar{\mathbf{q}}_{mb}^\top & \bar{q}_{mb,4} \end{bmatrix} \begin{bmatrix} -\frac{k}{2}\delta\theta_G \\ 1 \end{bmatrix} \right) \\
&= -((\hat{q}_{n,4}\mathbf{I}_{3\times 3} - [\hat{\mathbf{q}}_n])(\bar{q}_{mb,4}\mathbf{I}_{3\times 3} - [\bar{\mathbf{q}}_{mb}]) \\
&\quad + \hat{\mathbf{q}}_n\bar{\mathbf{q}}_{mb}^\top)^k\delta\theta_G + \text{other terms} \\
\Rightarrow \frac{\partial \mathbf{e}_\theta}{\partial^k\delta\theta_G} &= -((\hat{q}_{n,4}\mathbf{I}_{3\times 3} - [\hat{\mathbf{q}}_n])(\bar{q}_{mb,4}\mathbf{I}_{3\times 3} - [\bar{\mathbf{q}}_{mb}]) + \hat{\mathbf{q}}_n\bar{\mathbf{q}}_{mb}^\top) \quad (126)
\end{aligned}$$

where we have defined several intermediate quaternions, \hat{q}_r , \hat{q}_{rb} , \hat{q}_n , and \hat{q}_{mb} , for ease of notation. We compute the Jacobians of the remaining preintegrated measurements as follows (Eckenhoff, Geneva, and Huang, 2018):

$$\frac{\partial \mathbf{e}_{b_\omega}}{\partial \delta \mathbf{b}_{\omega_k}} = -\mathbf{I} \quad (127)$$

$$\frac{\partial \mathbf{e}_{b_\omega}}{\partial \delta \mathbf{b}_{\omega_{k+1}}} = \mathbf{I} \quad (128)$$

$$\frac{\partial \mathbf{e}_v}{\partial^k \delta \theta_G} = \left[{}^k\hat{\mathbf{R}}({}^G\hat{\mathbf{v}}_{k+1} - {}^G\hat{\mathbf{v}}_k + {}^G\mathbf{g}\Delta t) \right] \quad (129)$$

$$\frac{\partial \mathbf{e}_v}{\partial \delta \mathbf{b}_{\omega_k}} = -\mathbf{J}_\beta \quad (130)$$

$$\frac{\partial \mathbf{e}_v}{\partial^G \delta \mathbf{v}_k} = -{}^k\hat{\mathbf{R}} \quad (131)$$

$$\frac{\partial \mathbf{e}_v}{\partial^G \delta \mathbf{v}_{k+1}} = {}^k\hat{\mathbf{R}} \quad (132)$$

$$\frac{\partial \mathbf{e}_v}{\partial \delta \mathbf{b}_a} = -\mathbf{H}_\beta \quad (133)$$

$$\frac{\partial \mathbf{e}_{b_a}}{\partial \delta \mathbf{b}_{a_k}} = -\mathbf{I} \quad (134)$$

$$\frac{\partial \mathbf{e}_{b_a}}{\partial \delta \mathbf{b}_{a_{k+1}}} = \mathbf{I} \quad (135)$$

$$\frac{\partial \mathbf{e}_p}{\partial^k \delta \theta_G} = \left[{}^k\hat{\mathbf{R}} \left({}^G\hat{\mathbf{p}}_{k+1} - {}^G\hat{\mathbf{p}}_k - {}^G\hat{\mathbf{v}}_k\Delta t + \frac{1}{2}{}^G\mathbf{g}\Delta t^2 \right) \right] \quad (136)$$

$$\frac{\partial \mathbf{e}_p}{\partial \delta \mathbf{b}_{\omega_k}} = -\mathbf{J}_\alpha \quad (137)$$

$$\frac{\partial \mathbf{e}_p}{\partial^G \delta \mathbf{v}_k} = -{}^k\hat{\mathbf{R}}\Delta t \quad (138)$$

$$\frac{\partial \mathbf{e}_p}{\partial \delta \mathbf{b}_{a_k}} = -\mathbf{H}_\alpha \quad (139)$$

$$\frac{\partial \mathbf{e}_p}{\partial^G \delta \mathbf{p}_k} = -{}^k\hat{\mathbf{R}} \quad (140)$$

$$\frac{\partial \mathbf{e}_p}{\partial^G \delta \mathbf{p}_{k+1}} = {}^k\hat{\mathbf{R}} \quad (141)$$

A.2. Model 2 Measurement Jacobians

For Model 2, the orientation measurement Jacobians remain the same as in Model 1. For the remaining measurement Jacobians, we compute them in the same way as in Model 1 and are given by (see Equation (98)):

$$\frac{\partial \mathbf{e}_{b_\omega}}{\partial \delta \mathbf{b}_{\omega_k}} = -\mathbf{I} \quad (142)$$

$$\frac{\partial \mathbf{e}_{b_\omega}}{\partial \delta \mathbf{b}_{\omega_{k+1}}} = \mathbf{I} \quad (143)$$

$$\frac{\partial \mathbf{e}_v}{\partial^k \delta \theta_G} = [{}^k\hat{\mathbf{R}} ({}^G\hat{\mathbf{v}}_{k+1} - {}^G\hat{\mathbf{v}}_k)] - \mathbf{O}_\beta (\tilde{q}_4\mathbf{I} + [\tilde{\mathbf{q}}]) \quad (144)$$

$$\frac{\partial \mathbf{e}_v}{\partial \delta \mathbf{b}_{\omega_k}} = -\mathbf{J}_\beta \quad (145)$$

$$\frac{\partial \mathbf{e}_v}{\partial^G \delta \mathbf{v}_k} = -{}^k\hat{\mathbf{R}} \quad (146)$$

$$\frac{\partial \mathbf{e}_v}{\partial^G \delta \mathbf{v}_{k+1}} = {}^k\hat{\mathbf{R}} \quad (147)$$

$$\frac{\partial \mathbf{e}_v}{\partial \delta \mathbf{b}_{a_k}} = -\mathbf{H}_\beta \quad (148)$$

$$\frac{\partial \mathbf{e}_{b_a}}{\partial \delta \mathbf{b}_{a_{k+1}}} = \mathbf{I} \quad (149)$$

$$\frac{\partial \mathbf{e}_{b_a}}{\partial \delta \mathbf{b}_{a_k}} = -\mathbf{I} \quad (150)$$

$$\frac{\partial \mathbf{e}_p}{\partial^k \delta \theta_G} = [{}^k\hat{\mathbf{R}} ({}^G\hat{\mathbf{p}}_{k+1} - {}^G\hat{\mathbf{p}}_k - {}^G\hat{\mathbf{v}}_k\Delta T)] - \mathbf{O}_\alpha (\tilde{q}_4\mathbf{I} + [\tilde{\mathbf{q}}]) \quad (151)$$

$$\frac{\partial \mathbf{e}_p}{\partial \delta \mathbf{b}_{\omega_k}} = -\mathbf{J}_\alpha \quad (152)$$

$$\frac{\partial \mathbf{e}_p}{\partial^G \delta \mathbf{v}_k} = -{}^k\hat{\mathbf{R}}\Delta T \quad (153)$$

$$\frac{\partial \mathbf{e}_p}{\partial \delta \mathbf{b}_{a_k}} = -\mathbf{H}_\alpha \quad (154)$$

$$\frac{\partial \mathbf{e}_p}{\partial^G \delta \mathbf{p}_k} = -{}^k\hat{\mathbf{R}} \quad (155)$$

$$\frac{\partial \mathbf{e}_p}{\partial^G \delta \mathbf{p}_{k+1}} = {}^k\hat{\mathbf{R}} \quad (156)$$

where $[\tilde{\mathbf{q}}^\top \tilde{q}_4]^\top = {}^k\hat{\mathbf{q}} \otimes {}^k\hat{\mathbf{q}}^{\star-1}$

APPENDIX B: INVERSE-DEPTH MEASUREMENT JACOBIANS

We denote a and i the anchoring time step and the associated anchoring camera frame, respectively. Consider the case where we receive an image of the same feature at step k from camera j . This measurement can be divided into three categories: (i) when the measurement refers to both the anchoring time and camera that the inverse depth is being represented in; (ii) when the measurement refers to the same anchoring time, but a different camera; (iii) when the anchoring time and measurement time are distinct.

In case (i), we have (see Equation (106)):

$$\mathbf{h} = \begin{bmatrix} \alpha \\ \beta \\ 1 \end{bmatrix} \quad (157)$$

Then the measurement Jacobians are computed by (see Equations (101), (105) and (106)):

$$\frac{\partial \mathbf{e}_{fjk}}{\partial \alpha} = \mathbf{H}_{proj}(0, 0, 2, 1) \quad (158)$$

$$\frac{\partial \mathbf{e}_{fjk}}{\partial \beta} = \mathbf{H}_{proj}(0, 1, 2, 1) \quad (159)$$

$$\frac{\partial \mathbf{e}_{fjk}}{\partial \rho} = 0 \quad (160)$$

$$\mathbf{H}_{proj} = \begin{bmatrix} \frac{1}{h_3} & 0 & \frac{-h_1}{(h_3)^2} \\ 0 & \frac{1}{h_3} & \frac{-h_2}{(h_3)^2} \end{bmatrix} \quad (161)$$

where $\mathbf{H}_{proj}(i, j, k, l)$ refers to the block matrix of size (k, l) with starting index (i, j) .

In case (ii) where k refers to the same imaging time but a different camera (such as a stereo partner), we have (see Equation (106)):

$$\mathbf{h} = \begin{bmatrix} \alpha \\ \beta \\ 1 \end{bmatrix} + \rho^{C_j} \mathbf{p}_{C_i} \quad (162)$$

Because in this case the transformation parameters are rigid and known, we need only the derivatives with respect to the unknown feature parameterization:

$$\frac{\partial \mathbf{e}_{fjk}}{\partial \alpha} = [\mathbf{H}_{proj}^{C_j} \mathbf{R}_{C_i}^I] (0, 0, 2, 1) \quad (163)$$

$$\frac{\partial \mathbf{e}_{fjk}}{\partial \beta} = [\mathbf{H}_{proj}^{C_j} \mathbf{R}_{C_i}^I] (0, 1, 2, 1) \quad (164)$$

$$\frac{\partial \mathbf{e}_{fjk}}{\partial \rho} = C_j \mathbf{p}_{C_i} \quad (165)$$

In case (iii) where instead the measurement refers to a different time, we can write out the rigid transformation between the anchor and new current camera frame as follows:

$$\begin{aligned} {}^{C_{k,j}} \mathbf{p}_f &= {}^{C_{a,i}} \mathbf{R}^{C_{a,i}} \mathbf{p}_f + {}^{C_{k,j}} \mathbf{p}_{C_{a,i}} \\ &= \frac{1}{\rho} {}^{C_j} \mathbf{R}_G^k \mathbf{R}_a^G \mathbf{R}_{C_i}^I \mathbf{R} \begin{bmatrix} \alpha \\ \beta \\ 1 \end{bmatrix} + \\ &\quad {}^G \mathbf{R} ({}^G \mathbf{p}_{C_{a,i}} - {}^G \mathbf{p}_{C_{k,j}}) \\ &= \frac{1}{\rho} {}^{C_j} \mathbf{R}_G^k \mathbf{R}_a^G \mathbf{R}_{C_i}^I \mathbf{R} \begin{bmatrix} \alpha \\ \beta \\ 1 \end{bmatrix} + \end{aligned}$$

$$\begin{aligned} & {}^{C_j} \mathbf{R}_G^k \mathbf{R} ({}^G \mathbf{p}_a + {}^G \mathbf{R}^I \mathbf{p}_{C_i} - {}^G \mathbf{p}_k - {}^G \mathbf{R}^I \mathbf{p}_{C_j}) \\ &= {}^{C_j} \mathbf{R}_G^k \mathbf{R}_a^G \mathbf{R}_{C_i}^I \mathbf{R} \left(\frac{1}{\rho} \begin{bmatrix} \alpha \\ \beta \\ 1 \end{bmatrix} - {}^{C_i} \mathbf{p}_I \right) + \\ & {}^{C_j} \mathbf{R}_G^k \mathbf{R} ({}^G \mathbf{p}_a - {}^G \mathbf{p}_k) + {}^{C_j} \mathbf{p}_I \end{aligned} \quad (166)$$

With this, we have:

$$\begin{aligned} \mathbf{h} &= {}^{C_j} \mathbf{R}_G^k \mathbf{R}_a^G \mathbf{R}_{C_i}^I \mathbf{R} \left(\begin{bmatrix} \alpha \\ \beta \\ 1 \end{bmatrix} - \rho^{C_i} \mathbf{p}_I \right) + \\ & \rho_I^{C_j} \mathbf{R}_G^k \mathbf{R} ({}^G \mathbf{p}_a - {}^G \mathbf{p}_k) + \rho^{C_j} \mathbf{p}_I \end{aligned} \quad (167)$$

We can then take the derivative with respect to each variable:

$$\frac{\partial \mathbf{e}_{fjk}}{\partial {}^a \delta \boldsymbol{\theta}_G} = -\mathbf{H}_{proj} {}^{C_j} \mathbf{R}_G^k \mathbf{R}_a^G \mathbf{R} \left[{}^{C_i} \mathbf{R} \left(\begin{bmatrix} \alpha \\ \beta \\ 1 \end{bmatrix} - \rho^{C_i} \mathbf{p}_I \right) \right] \quad (168)$$

$$\frac{\partial \mathbf{e}_{fjk}}{\partial {}^G \mathbf{p}_a} = \mathbf{H}_{proj} \rho_I^{C_j} \mathbf{R}_G^k \mathbf{R} \quad (169)$$

$$\begin{aligned} \frac{\partial \mathbf{e}_{fjk}}{\partial {}^k \delta \boldsymbol{\theta}_G} &= \mathbf{H}_{proj} {}^{C_j} \mathbf{R} \left[{}^k \mathbf{R}_a^G \mathbf{R}_{C_i}^I \mathbf{R} \left(\begin{bmatrix} \alpha \\ \beta \\ 1 \end{bmatrix} - \rho^{C_i} \mathbf{p}_I \right) + \right. \\ & \left. \rho_G^k \mathbf{R} ({}^G \mathbf{p}_a - {}^G \mathbf{p}_k) \right] \end{aligned} \quad (170)$$

$$\frac{\partial \mathbf{e}_{fjk}}{\partial {}^G \mathbf{p}_k} = -\mathbf{H}_{proj} \rho_I^{C_j} \mathbf{R}_G^k \mathbf{R} \quad (171)$$

$$\frac{\partial \mathbf{e}_{fjk}}{\partial \alpha} = [\mathbf{H}_{proj} {}^{C_j} \mathbf{R}_G^k \mathbf{R}_a^G \mathbf{R}_{C_i}^I] (0, 0, 2, 1) \quad (172)$$

$$\frac{\partial \mathbf{e}_{fjk}}{\partial \beta} = [\mathbf{H}_{proj} {}^{C_j} \mathbf{R}_G^k \mathbf{R}_a^G \mathbf{R}_{C_i}^I] (0, 1, 2, 1) \quad (173)$$

$$\begin{aligned} \frac{\partial \mathbf{e}_{fjk}}{\partial \rho} &= \mathbf{H}_{proj} (-{}^{C_j} \mathbf{R}_G^k \mathbf{R}_a^G \mathbf{R}_{C_i}^I \mathbf{R}^{C_i} \mathbf{p}_I + \\ & {}^{C_j} \mathbf{R}_G^k \mathbf{R} ({}^G \mathbf{p}_a - {}^G \mathbf{p}_k) + {}^{C_j} \mathbf{p}_I) \end{aligned} \quad (174)$$

APPENDIX C: RELATIVE-POSE MEASUREMENT JACOBIAN

Recall that in Equation (120), j denotes the query image and k is the keyframe. We partition the relative-pose residual \mathbf{e}_d into the relative-orientation residual \mathbf{e}_θ and the relative-position residual \mathbf{e}_p . The Jacobians with respect to the states can be found by perturbation in the same way as before.

$$\begin{aligned} \mathbf{e}_\theta &= 2\mathbf{vec} \left(\begin{bmatrix} \frac{j \delta \boldsymbol{\theta}_G}{2} \\ 1 \end{bmatrix} \otimes {}^j \hat{q} \otimes {}^k \hat{q}^{-1} \otimes {}^j \check{q}^{-1} \right) \\ &= 2\mathbf{vec} \left(\mathcal{R} \left({}^j \hat{q} \otimes {}^k \hat{q}^{-1} \otimes {}^j \check{q}^{-1} \right) \begin{bmatrix} \frac{j \delta \boldsymbol{\theta}_G}{2} \\ 1 \end{bmatrix} \right) \\ &= (\bar{q}_{r,4} \mathbf{I} + [\mathbf{q}_r])^j \delta \boldsymbol{\theta}_G + \dots \\ \Rightarrow \frac{\partial \mathbf{e}_\theta}{\partial {}^j \delta \boldsymbol{\theta}_G} &= (\bar{q}_{r,4} \mathbf{I} + [\mathbf{q}_r]) \end{aligned} \quad (175)$$

Similarly, we perturb the quaternion estimate of the keyframe to compute the corresponding Jacobian as:

$$\begin{aligned} \mathbf{e}_\theta &= 2\mathbf{vec} \left({}^j \hat{q} \otimes {}^k \hat{q}^{-1} \otimes \begin{bmatrix} \frac{-k \delta \boldsymbol{\theta}_G}{2} \\ 1 \end{bmatrix} \otimes {}^j \check{q}^{-1} \right) \\ &= 2\mathbf{vec} \left(\mathcal{L} \left({}^j \hat{q} \right) \mathcal{R} \left({}^k \check{q} \right)^\top \begin{bmatrix} \frac{-k \delta \boldsymbol{\theta}_G}{2} \\ 1 \end{bmatrix} \right) = \end{aligned}$$

$$\begin{aligned}
& - \left(\left({}^j\hat{q}_4\mathbf{I} - \lfloor {}^j\hat{\mathbf{q}} \rfloor \right) \left({}^j\check{q}_4\mathbf{I} - \lfloor {}^j\check{\mathbf{q}} \rfloor \right) + {}^j\hat{\mathbf{q}}_k {}^j\check{\mathbf{q}}^{\top} \right)^k \delta \boldsymbol{\theta}_G + \dots \\
& \Rightarrow \frac{\partial \mathbf{e}_{\theta}}{\partial^k \delta \boldsymbol{\theta}_G} = - \left(\left({}^j\hat{q}_4\mathbf{I} - \lfloor {}^j\hat{\mathbf{q}} \rfloor \right) \left({}^j\check{q}_4\mathbf{I} - \lfloor {}^j\check{\mathbf{q}} \rfloor \right) + {}^j\hat{\mathbf{q}}_k {}^j\check{\mathbf{q}}^{\top} \right)
\end{aligned}$$

Again by following a similar procedure, we can find the Jacobians of the relative-position residual with respect to the state as follows (see Eckenhoff, Geneva, and Huang (2018)):

$$\frac{\partial \mathbf{e}_p}{\partial^G \delta \mathbf{p}_j} = {}^k_G \hat{\mathbf{R}} \quad (176)$$

$$\frac{\partial \mathbf{e}_p}{\partial^G \delta \mathbf{p}_k} = - {}^k_G \hat{\mathbf{R}} \quad (177)$$

$$\frac{\partial \mathbf{e}_p}{\partial^k \delta \boldsymbol{\theta}_G} = \lfloor {}^k_G \hat{\mathbf{R}} ({}^G \mathbf{p}_j - {}^G \mathbf{p}_k) \rfloor \quad (178)$$